Ten3–Lphn2-mediated target selection across the extended hippocampal network demonstrates a repeated strategy for circuit assembly

Ellen C. Gingrich[1,2], Daniel T. Pederick[1,3], Yanbo Zhang[1], Liqun Luo[1]
[1]Department of Biology, Howard Hughes Medical Institute, Stanford University, Stanford, CA, 94305, USA
[2]Neurosciences Interdepartmental PhD Program, Stanford University, Stanford, CA, 94305, USA
[3]Present address: Department of Neuroscience, Johns Hopkins University School of Medicine, Baltimore, MD, USA

SUMMARY

How do thousands of cell-surface proteins specify billions of neuronal connections in developing brains? We previously found that inverse expression of a ligand–receptor pair, teneurin-3 (Ten3) and latrophilin-2 (Lphn2) in CA1 and subiculum, instructs CA1→subiculum target selection through Ten3–Ten3 homophilic attraction and Ten3–Lphn2 heterophilic reciprocal repulsions. Here, we leveraged conditional knockouts to systematically demonstrate that these mechanisms generalize to extended hippocampal networks, including entorhinal cortex and hypothalamus. Cooperation between attraction and repulsion differs depending on the order in which developing axons encounter the attractant and repellent subfields. Strikingly, Ten3 and Lphn2 can serve both as ligands for incoming axons and receptors for their own target selection, within the same neuron; Ten3 can be repulsive or attractive as ligand or receptor. Thus, multifunctionality and repeated use, together with recurrent circuit motifs prevalent in the brain, enable one ligand–receptor pair to instruct target selection of many more neurons.

INTRODUCTION

During development, neural circuits must self-assemble with exquisite wiring precision to enable normal cognition and behavior, including functions such as memory and spatial navigation. Roger Sperry proposed in his chemoaffinity hypothesis that, to accomplish this feat, individual neurons carry unique molecular identification tags that distinguish themselves from neighboring neurons.[1] Many such cell-surface proteins (CSPs) have since been identified as critical regulators of axon guidance and target selection.[2,3] These CSPs can be expressed on both pre- and post-synaptic cells and use mechanisms of attraction and repulsion to specify neuronal partner matching.[4–13]

The human brain, however, contains ~10^{11} neurons, each making thousands of synaptic connections, but fewer than 3000 CSPs that can be leveraged to instruct wiring.[14–17] This presents a challenge to the developing brain, as the number of connections to specify vastly outnumbers the genes available to instruct them, precluding the possibility that each neuron carries a unique tag. Among multiple strategies that have been proposed to overcome this discrepancy, one is to re-use the same CSPs at spatially distinct locations.[18] For example, the ligand–receptor pair, ephrin-A–EphA, have inverse expression in several retinotopic nodes of the visual circuit including the retina, superior colliculus (SC), lateral geniculate nucleus (LGN), and the primary visual cortex (V1).[19] In the retina→SC connection, ephrin-A–EphA-mediated reciprocal repulsion during target selection has been shown to establish the precise anterior–posterior retinotopy.[5,6,20–22] However, although ephrin-A–EphA signaling is hypothesized to directly regulate retinotopic connectivity across other nodes, this has not been directly studied beyond how retina→SC mis-wiring can effect downstream visual circuitry.[23] Additionally, there is a shortage of tissue-specific loss-of-function studies that interrogate the roles of ephrin-A and EphA in axons and targets independently to distinguish pre- versus post-synaptic effects. Indeed, the only study employing conditional knockout (of ephrin-A5) we are aware of uncovered the importance of target-independent axon-axon interactions in establishing retinocollicular connectivity.[24]

Compared to sensory and motor systems, much less is known about wiring mechanisms of circuits in the central brain. One circuit in the central brain with well-characterized topographic projections across multiple

nodes is the extended hippocampal network (**Figure 1A$_{1–2}$**). The medial and lateral hippocampal subnetworks (MHN and LHN) preferentially process spatial and object-related information, respectively.[25,26] The MHN consists, in part, of medial entorhinal cortex (MEC), proximal CA1 (pCA1), distal subiculum (dSub), and lateral subdivision of the medial mammillary nucleus (lat-mMN) of the hypothalamus, which are interconnected with each other. Conversely, the LHN consists of interconnected lateral entorhinal cortex (LEC), distal CA1 (dCA1), proximal subiculum (pSub), and medial mMN (med-mMN) (**Figure 1A**).[27–33]

We previously found a CSP pair, teneurin-3 (Ten3) and latrophilin-2 (Lphn2), that exhibit inverse expression in both CA1 and subiculum, such that the interconnected regions of pCA1→dSub and dCA1→pSub express Ten3 and Lphn2, respectively (**Figure 1A$_{1-2}$**).[8,9] Genetic loss- and gain-of-function analyses revealed that the CA1→subiculum specificity is produced by the cooperation between homophilic Ten3–Ten3-mediated attraction and heterophilic Ten3–Lphn2-mediated reciprocal repulsions (**Figure 1A$_3$**).[9,34] Given that Ten3 and Lphn2 also exhibit inverse expression in other nodes of the MHN and LHN including entorhinal cortex (EC) and medial mammillary nucleus (mMN),[8,9,35,36] here we address whether other parts of the network follow a 'Ten3→Ten3, Lphn2→Lphn2' connectivity rule and, if so, whether this ligand–receptor pair is used repeatedly to instruct the precise assembly at other nodes of the network using systematic conditional knockout analyses.

RESULTS

The extended hippocampal network follows a 'Ten3→Ten3, Lphn2→Lphn2' connectivity rule

Beyond its inverse expression in CA1 and subiculum, Ten3 is also enriched in subfields of several other nodes in the extended hippocampal network, including MEC and lat-mMN.[8,36] Conversely, Lphn2 is known to be enriched in LEC (**Figure 1A**).[9,35,36] Immunostaining for tagged Ten3 and Lphn2 (in *Ten3$^{HA/HA}$;Lphn2$^{mVenus/mVenus}$* knockin mice[37,38]) confirmed the striking inverse expression of these two proteins at postnatal day 8 (P8). As previously reported, Ten3 protein is enriched in pCA1, dSub, MEC, and lat-mMN; by contrast, Lphn2 protein is enriched in dCA1, pSub, LEC, and med-mMN (**Figure 1A, B**).[8,9,35] Given this topographically-restricted expression, we considered whether these two CSPs may serve a broader role in assembling the extended hippocampal networks than previously appreciated.

Previous studies have focused on the relationship between Ten3–Lphn2 inverse expression and connection topography in the hippocampal-entorhinal circuitry.[8,9,35] To further investigate this relationship in hippocampal outputs to the hypothalamus, we injected adeno-associated viruses (AAVs) as anterograde tracers into neighboring locations in the subiculum (*AAV-GFP* into Lphn2-high pSub, *AAV-mCherry* (*mCh*) into Ten3-high dSub) and assessed their projections to mMN (**Figure 1C**, **Figure S1A**). Note that in this study, pSub will refer to the entirety of the Lphn2-high region of subiculum which anatomically constitutes approximately 75% of the length of subiculum (**Figure S1A$_1$**).[9] We found that GFP$^+$ axons were restricted to Lphn2-high med-mMN whereas mCh$^+$ axons filled Ten3-high lat-mMN (**Figure 1C$_2$**, **Figure S1A$_2$, B**), validating that the 'Ten3→Ten3, Lphn2→Lphn2' connectivity rule also applies to subiculum→mMN projection, analogous to projections between CA1, subiculum, and entorhinal cortex (**Figure 1A$_{1, 2}$**).[8,9] The axons from subiculum to mMN, however, did not appear to be topographically segregated, instead forming a uniform bundle that only splits into the appropriate subfield as it enters the mMN target region (**Figure S1B**).

Spatiotemporal patterns of Ten3 and Lphn2 expression with respect to target entry of developing axons

To instruct target selection of axons connecting these nodes, Ten3 and Lphn2 must be inversely expressed at each node prior to the maturation of the circuit. To establish expression onset, we performed dual *in situ* hybridization for *Ten3* and *Lphn2* mRNA using RNAScope[39] across multiple developmental timepoints. At E15.5, *Ten3* and *Lphn2* were already inversely expressed in mMN (**Figure 1E**) but exhibited minimal expression in the hippocampal and entorhinal regions. By E17.5, *Ten3* was highly expressed in entorhinal cortex whereas *Lphn2* expression remained low (**Figure 1D$_1$**), marking this as the only case we observed where *Ten3–Lphn2* were not inversely expressed at onset. By P0, CA1, subiculum, and entorhinal cortex all exhibited inverse expression, resembling protein staining at P8 (**Figure 1B$_1$, D$_2$**) and in previous studies.[9,36] *Ex vivo* tracing from MEC showed

that axons began to invade dSub at E17.5 and increased in density through P0 (**Figure S1C, D**), roughly aligning with the onset of *Ten3* and *Lphn2* expression in dSub and pSub, respectively. Although little is known about the timing of subiculum→mMN axon targeting, expression of *Ten3* and *Lphn2* in the subiculum axon bundle in the whole-brain staining described in our manuscript[37] indicated these axons reach mMN around P0. Since each node of the circuit expressed *Ten3* and *Lphn2* mRNA (**Figure 1D, E**), the protein distribution we observed (**Figure 1B**) is likely contributed to by both input axons and target neurons, further reinforcing the prevalence of like–like connectivity.

Although each of the four nodes we examined—CA1, subiculum, entorhinal cortex, and mMN—exhibited striking inverse expression of Ten3 and Lphn2, the spatial organization of developing axons encountering each target node in relation to the expression pattern could influence target selection strategy. By re-examining our previous study,[8] characterizing adult axon entry routes,[40–42] performing developmental tracing, and cataloguing Ten3–Lphn2 protein expression, we established three distinct spatial configurations in which axons may encounter Ten3 and Lphn2 subfields in the target (**Figure 1F**; **Figure S1B, E–G**). (1) For CA1→subiculum at P2, Ten3$^+$ pCA1 axons first encounter the Lphn2$^+$ pSub, then the Ten3$^+$ dSub (**Figure 1F, left**)[8], consistent with adult single axon tracing studies.[41,42] (2) For entorhinal cortex→subiculum, Ten3$^+$ MEC axons first encountered the Ten3$^+$ dSub, then the Lphn2$^+$ pSub, as apparent in *ex vivo* tracing of MEC in P0 *Ten3$^{HA/HA}$;Lphn2$^{mV/mV}$* pups (**Figure 1F, middle**; **Figure S1E**). This is also consistent with adult single axon tracing from entorhinal cortex.[40,43,44] (3) For subiculum→mMN, Ten3$^+$ dSub axons encountered the Ten3$^+$ lat-mMN and Lphn2$^+$ med-mMN subfields simultaneously, confronting them with a more binary choice (**Figure 1F, right**; **Figure S1B, F, G**). Likewise, Lphn2$^+$ pSub axons encountered Ten3$^+$ and Lphn2$^+$ subfields simultaneously (**Figure S1B, F, G**). Our previous work has established that both Ten3–Ten3 homophilic attraction and Ten3–Lphn2 heterophilic reciprocal repulsion are critical in the first scenario (**Figure 1F, left**). However, it remains unclear how the other two configurations of developing axons encountering the Ten3$^+$ or Lphn2$^+$ target subfields (**Figure 1F, middle and right**) may influence the use of these mechanisms.

Ten3 is required in MEC axons for their precise targeting to dSub

Ten3–Ten3 homophilic attraction and Lphn2–Ten3 heterophilic repulsion are critical for establishing the appropriate topography of the pCA1→dSub connection (**Figure 1A$_3$**).[9] To determine if these mechanisms are re-used at the MEC→dSub connection, we first asked if Ten3 is required in MEC axons for targeting using a conditional knockout strategy. We injected *Cre-GFP*-expressing lentivirus into MEC of postnatal day 0 (P0) wildtype or *Ten3$^{fl/fl}$* pups, titrating the concentration to allow for a roughly even proportion of Cre$^+$ and Cre$^-$ neurons (**Figure 2A, left**). At P42 or older, we subsequently injected a mix of anterograde *AAV-CreON-GFP* and *AAV-CreOFF-mCh* into MEC of these mice (**Figure 2A, middle**) to assess the targeting of control and *Ten3*-null axons within the same animal (**Figure 2A, right**). Injections were restricted to within the most medial 20% of entorhinal cortex to ensure tracing of mostly Ten3$^+$ axons (**Figure 2B**).

In *Ten3$^{+/+}$* controls, mCh$^+$ (Cre$^-$) and GFP$^+$ (Cre$^+$) MEC neurons alike exclusively projected to the distal, Ten3-high region of the subiculum (**Figure 2C, D, G**). However, in *Ten3$^{fl/fl}$* mice, mCh$^+$ axons (Cre$^-$, functionally wildtype) remained restricted to Ten3-high dSub, whereas GFP$^+$ (Cre$^+$, *Ten3* conditionally knocked out, or *Ten3^{MEC}-cKO*) axons invaded Lphn2-high regions of pSub (**Figure 2E, F, H**). Quantification of axon fluorescence intensity (FI) showed that only GFP$^+$ axons in *Ten3$^{fl/fl}$* mice had a proximal shift along the distal–proximal axis of the subiculum (**Figure 2G$_1$, H$_1$**). This shift resulted in lower axon density in the appropriate Ten3-high dSub and increased density in the Lphn2-high pSub (**Figure 2G$_2$, H$_2$**). This mistargeting also caused GFP$^+$ axons to cover a larger region of subiculum, as evidenced by area under the curve of FI traces, when Cre$^-$ and Cre$^+$ projections were compared pairwise within animals (**Figure 2I**). A similar phenotype was observed for target selection of MEC axons in CA1: GFP$^+$ (and *Ten3^{MEC}-cKO*) axons in *Ten3$^{fl/fl}$* mice spread more distally into Lphn2-high regions compared to mCh$^+$ wildtype axons (**Figure S2A–D**).

MEC axons also have topographic projections to contralateral dSub and pCA1 that could be affected by *Ten3^{MEC}-cKO*. Although these projections are much sparser than the ipsilateral connection and were not observable in every animal, qualitatively, GFP$^+$ axons also mistargeted into Lphn2-high regions of pSub and

dCA1 in *Ten3*$^{fl/fl}$ mice compared to mCh^{+} axons in *Ten3*$^{fl/fl}$ mice or GFP^{+} and mCh^{+} axons in *Ten3*$^{+/+}$ control mice (**Figure 2K, L**; **Figure S2F**). These observations suggest that ipsi- and contralateral projections use similar mechanisms for subfield selection. Taken together, these data demonstrated that Ten3 is required in MEC neurons for their axons to precisely target to dSub and pCA1 (**Figure 2J, M**; **Figure S2E, G**).

Ten3 and Lphn2 in subiculum cooperate to instruct the precise targeting of MEC axons

We next asked whether Ten3 and/or Lphn2 are required in the subiculum target neurons, in addition to requiring Ten3 in MEC axons, for the MEC→dSub projection. We used a pan-subiculum Cre driver, *Nts-Cre*, which exhibits dense expression in subiculum at P0 (**Figure 3A**; **Figure S3A**) but minimal expression in entorhinal cortex or CA1 (**Figure S3A, B**), to conditionally knockout *Ten3*, *Lphn2*, or both selectively in subiculum but not in entorhinal cortex or CA1.

We labeled MEC→dSub axon projections by injecting *AAV-CreOFF-mCh* into MEC (**Figure 3B, C**). To examine if target deletions could recapitulate the phenotype observed in *Ten3*^{MEC}*-cKO* (**Figure 2J**; which presumably lose both Ten3–Ten3 attraction and Lphn2–Ten3 repulsion), we started by assessing axon distributions in *Ten3* and *Lphn2* double cKO mice. In *Nts-Cre;Ten3*$^{fl/fl}$*;Lphn2*$^{fl/fl}$ (*Ten3*^{Sub}*/Lphn2*^{Sub}-cKO) mice, we observed mistargeting of Ten3^{+} axons into the Lphn2-high subfield of subiculum compared to *Ten3*$^{fl/fl}$*;Lphn2*$^{fl/fl}$ littermate controls (**Figure 3D–G**). By contrast, we did not observe mistargeting of MEC→pCA1 axon in the same experiment (**Figure S4A–C**), reinforcing the specificity of *Nts-Cre* for subiculum-restricted manipulations. These experiments demonstrated that Ten3 and/or Lphn2 are required in the subiculum target for Ten3^{+} MEC axons to target to Ten3^{+} dSub, through Ten3–Ten3 homophilic attraction, Lphn2–Ten3 heterophilic repulsion, or a combination.

To examine the relative contribution of Ten3–Ten3 homophilic attraction and Lphn2–Ten3 heterophilic repulsion, we repeated these experiments with single cKOs: (1) *Nts-Cre;Lphn2*$^{fl/fl}$ (*Lphn2*^{Sub}-cKO; with *Nts-Cre;Lphn2*$^{+/+}$ littermate controls); and (2) *Nts-Cre;Ten3*$^{fl/fl}$ (*Ten3*^{Sub}-cKO; with *Nts-Cre;Ten3*$^{+/+}$ littermate controls). As expected, CA1 targeting was normal under both conditions (**Figure S4D, E**). Unexpectedly, however, Ten3^{+} MEC axons appeared to target the appropriate subiculum region in both single knockout conditions (**Figure 3H–K**).

These data suggest that Ten3–Ten3-mediated attraction and Lphn2–Ten3-mediated repulsion are largely redundant, with each mechanism compensating for the loss of the other (**Figure 3L**). This is contrary to our previous studies of pCA1→dSub targeting, where conditional knockout of either *Ten3* (attraction) or *Lphn2* (repulsion) in the subiculum target produces mistargeting phenotypes.[8,9] One possibility is that, unlike the pCA1→dSub projection where axons encounter a large Lphn2-high region of pSub before contacting the appropriate dSub target, in the MEC→dSub projection, MEC axons projecting to dSub encounter the Ten3 attractant first (**Figure 1F**, **Figure S1E**), such that attraction alone may stabilize MEC axons before they reach the Lphn2-high pSub. Conversely, even without attraction, the repulsive forces emanating from Lphn2 are sufficient to preclude axons from entering pSub. Only when both Ten3 and Lphn2 are removed from the target do MEC axons phenocopy loss of Ten3 in axons, supporting that Ten3–Ten3 attraction and Lphn2–Ten3 repulsion cooperate in mediating MEC→dSub target selection.

Ten3 is required in subiculum for dSub axons to precisely target to lateral mMN

Our data reveal that the precise targeting of pCA1→dSub and MEC→dSub both require the cooperation of Ten3–Ten3 attraction and Lphn2–Ten3 repulsion, but differ in their degree of reliance on these mechanisms individually, in accordance with the order in which Ten3^{+} axons encounter Ten3^{+} or Lphn2^{+} subfields. Given this heterogeneity, we next asked what happens during a third scenario where axons encounter Ten3 and Lphn2 concurrently, as seen in dSub→lat-mMN connection (**Figure 1F**; **Figure S1F, G**).

We first assessed if Ten3 is required in dSub axons for appropriate targeting to lat-mMN by tracing dSub axons in *Ten3*^{Sub}-cKO mice using the same *Nts-Cre* driver as above (**Figure 4A, B**). Note that unlike in Figure 3, where *Ten3*^{Sub}-cKO was used to examine the consequence of <u>target</u> deletion for MEC→dSub projection, hereafter we leveraged *Ten3*^{Sub}-cKO to examine the consequence of <u>axon</u> deletion for subiculum→mMN projection. In

control animals, dSub axons were restricted to the Ten3-high lateral region of mMN (lat-mMN; **Figure 4C, D**). However, in *Ten3*^{Sub}-cKO animals, some dSub axons spread into Lphn2-high med-mMN (**Figure 4E, F**). Because the mMN cannot be easily approximated as a linear structure, in contrast to hippocampal and entorhinal regions, we quantified axon mistargeting by defining the lat-mMN and med-mMN boundaries using DAPI counterstaining **(Figure S5H)** and calculating the fraction of fluorescence intensity in med-mMN of total fluorescence intensity. In control animals, axons were predominantly restricted to the lat-mMN, whereas in *Ten3*^{Sub}-cKO, the fraction of axons in med-mMN significantly increased (**Figure 4G**).

Even in an independent cohort of animals with relatively weaker and more distally restricted injection sites (**Figure S5A, C, E**), individual aberrant axons can be seen straying outside of lat-mMN into Lphn2-high med-mMN in *Ten3*^{Sub}-cKO animals relative to controls (**Figure S5B, D**). Rather than quantifying fluorescence intensity, these animals were rank-ordered by severity of mistargeting. This analysis showed that *Ten3*^{Sub}-cKO animals consistently ranked as having more mistargeting (**Figure S5F$_1$**). This sparse labeling of *Ten3*-null axons showed that individual axons could mistarget as far as the most anterior-medial border of med-mMN (i.e., the Lphn2-high region furthest from Ten3-high lat-mMN) and did not exclusively mistarget to the bordering Lphn2-high subfield, as seen in MEC→dSub. We also observed this dSub axonal spread to med-mMN as these projections cross the midline into contralateral mMN, suggesting that once the targeting is disrupted, the axons remain in the incorrect subfield (**Figure 4I; Figure S5F$_2$**). Thus, Ten3 is required in dSub axons to precisely target lat-mMN (**Figure 4H**).

Lphn2 is required in mMN for the precise targeting of dSub axons to lat-mMN

Given that Ten3 is required in dSub axons for them to appropriately target to mMN, analogous to its role in the pCA1→dSub and MEC→dSub connections, we next asked whether Ten3 and/or Lphn2 are also required in the mMN target. To do this, we used *Sim1-Cre*, a Cre driver with dense expression in mMN as early as E15.5 (**Figure 5A**, **Figure S3D**), but minimal expression in subiculum (**Figure S3E**).

We injected *AAV-mCh* into dSub to assess dSub→lat-mMN axon projections and, again, started by assessing *Sim1-Cre;Ten3*$^{fl/fl}$*;Lphn2*$^{fl/fl}$ (*Ten3*^{mMN}*/Lphn2*^{mMN}-cKO) animals to determine if the Ten3 axonal deletion phenotype is recapitulated by *Ten3* and *Lphn2* double cKO in the target (**Figure 5B, C**). In *Ten3*^{mMN}*/Lphn2*^{mMN}-cKO animals, we observed mistargeting of the Ten3$^+$ dSub axons into the Lphn2-high med-mMN when compared to *Ten3*$^{fl/fl}$*;Lphn2*$^{fl/fl}$ control (**Figure 5D–G**). This mistargeting was also observed in contralateral mMN of *Ten3*^{mMN}*/Lphn2*^{mMN}-cKO (**Figure S6A, B**). This experiment demonstrated that Ten3 and/or Lphn2 is required in mMN for the appropriate targeting of Ten3$^+$ dSub axons.

To determine the relative contribution of Lphn2 and Ten3 to the double target knockout phenotype, we repeated these experiments with *Lphn2* or *Ten3* single cKOs in the mMN target. Similar to the *Ten3*^{mMN}*/Lphn2*^{mMN}-cKO, Ten3$^+$ dSub axons mistargeted to med-mMN in *Lphn2*^{mMN}-cKO animals as well, causing an increase in the density of axons in med-mMN relative to the appropriate lat-mMN target (**Figure 5H, I**). However, dSub axons in *Ten3*^{mMN}-cKO still predominantly targeted lat-mMN (**Figure 5J, K**). These phenotypes were recapitulated in contralateral mMN with mistargeting in *Lphn2*^{mMN}-cKO, but not *Ten3*^{mMN}-cKO animals (**Figure S6C, D**).

Taken together, these results suggested that Lphn2–Ten3-mediated repulsion is required in the dSub→lat-mMN connection (**Figure 5L**, **Figure S6E**). Additionally, the mistargeting phenotype in *Lphn2*^{mMN}-cKO animals implied that, like in pCA1→dSub, Ten3-mediated attraction alone cannot compensate for the loss of Lphn2-mediated repulsion for the appropriate targeting of Ten3$^+$ axons.

Lphn2 is required in subiculum for precise targeting of pSub axons to med-mMN

So far, we have focused on connections between target selection of Ten3$^+$ axons in the medial subdivision of the extended hippocampal network (**Figure 1A**). However, in the dCA1→pSub (the lateral subfields of the CA1→subiculum connection), Lphn2$^+$ CA1 axons are repelled by Ten3 in dSub, meaning Ten3–Lphn2 heterophilic repulsions are reciprocal, with both Ten3 and Lphn2 capable of acting as receptor and ligand (**Figure 1A$_3$**).[9] Therefore, we asked whether reciprocal repulsions are also generalizable to other nodes in the extended

hippocampal network. We used pSub→med-mMN, the Lphn2-high subdivision of the subiculum→mMN connection, to address this question.

Modifying the experiments in Figure 4 for examining Lphn2^{+} axons, we injected *AAV-CreON-GFP* into pSub of *Nts-Cre;Lphn2*$^{+/+}$ controls and *Nts-Cre;Lphn2*$^{fl/fl}$ (*Lphn2*^{Sub}-cKO) mice (**Figure 6A, B**). In control animals, pSub axons were restricted to the med-mMN whereas aberrant pSub axons strayed into lat-mMN in *Lphn2*^{Sub}-cKO (**Figure 6C–F**). Although this phenotype was more subtle than when *Ten3* was deleted in dSub axons, there was a significant increase of axon density in Ten3-high lat-mMN in *Lphn2*^{Sub}-cKO compared to control (**Figure 6G**). This phenotype was also present in contralateral mMN (**Figure 6I**). These data demonstrate that Lphn2 is required in subiculum for pSub axons to precisely target med-mMN (**Figure 6H**).

Target requirement for the pSub→med-mMN projection

To determine if Ten3–Lphn2 are required in the mMN target for the appropriate targeting of pSub→med-mMN and, thus, recapitulate the *Lphn2*^{Sub}-cKO phenotype, we injected *AAV-GFP* into pSub of *Sim1-Cre;Ten3*$^{fl/fl}$*;Lphn2*$^{fl/fl}$ (*Ten3*^{mMN}*/Lphn2*^{mMN}-cKO) animals (**Figure 7A, B**). Indeed, in *Ten3*^{mMN}*/Lphn2*^{mMN}-cKO animals, we observed aberrant Lphn2^{+} pSub axons in the Ten3-high lat-mMN when compared to *Ten3*$^{fl/fl}$*;Lphn2*$^{fl/fl}$ controls (**Figure 7C–G**), including in contralateral mMN (**Figure 7I**), recapitulating the spreading phenotype of *Lphn2* deletion in subiculum axons (**Figure 6**). Because Lphn2 does not exhibit homophilic binding,[9,45] we did not test single cKOs as it is unlikely that loss of Lphn2 in the target contributes to the phenotype in *Ten3*^{mMN}*/Lphn2*^{mMN}-cKOs.

Taken together, these data suggest that Ten3–Lphn2 heterophilic repulsion is required to correctly specify pSub→med-mMN (**Figure 7H**) and that this repulsion is reciprocal within the subiculum→mMN connection, as in the CA1→subiculum connection[9] (**Figure 7J**).

DISCUSSION

Here, we use the topographic connections of the extended hippocampal network to examine whether the same ligand–receptor pair can be re-used for target selection for multiple connections within the same network. Our systematic conditional knockout approach demonstrated that Ten3–Ten3 homophilic attraction and Ten3–Lphn2 heterophilic reciprocal repulsion (**Figure 7J**) instruct target selection within the extended hippocampal network—MEC→dSub/pCA1, dSub→lat-mMN, and pSub→med-mMN, in addition to previously reported CA1→subiculum connections.[8,9] To our knowledge, this is the first time a ligand–receptor pair has been shown to instruct target selection in multiple nodes of the same network. Our analysis of conditional target deletions also revealed differential requirements of repulsion and attraction in different nodes depending on the order in which developing axons encounter the attractant versus the repellent subfield in the target (**Figure 1F**).

Differential requirement of attraction and repulsion at different circuit nodes

In the pCA1→dSub connection, our previous studies indicated that target deletion of *Lphn2* alone caused spread of pCA1 axons to pSub, and target deletion of both *Lphn2* and *Ten3* exhibited more severe pCA1 axon spreading to pSub.[9] Thus, Lphn2–Ten3 repulsion is by itself required for preventing pCA1 axon mistargeting. This is likely because Ten3^{+} pCA1 axons first encounter the Lphn2^{+} pSub subfield before Ten3^{+} dSub subfield (**Figure 1F, left**), making repulsion necessary to prevent axons stalling before they find the attractive subfield.

By contrast, our data indicates that conditional target deletion of *Lphn*2 did not cause a significant targeting defect in the MEC→dSub connection (**Figure 3I**). Only when we deleted both *Ten3* and *Lphn2* in the subiculum target did we recapitulate *Ten3* deletion in MEC axon (**Figure 3G**, compared to **Figure 2H**). (Subiculum deletion of *Ten3* and *Lphn2* has a slightly weaker phenotype than *Ten3* deletion in MEC axons possibly due to the late onset of *Nts-Cre,* between E17.5 and P0, such that some target proteins may have already been produced before conditional gene knockout.) Our developmental axon tracing indicated that MEC axons first encountered Ten3^{+} dSub before encountering Lphn2^{+} pSub (**Figure 1F, middle**; **Figure S1D, E**). Thus, the simplest interpretation for the lack of phenotype of *Lphn2* target deletion in the MEC→dSub connection is that

Ten3–Ten3 homophilic attraction is largely sufficient to retain MEC axons in the Ten3$^+$ dSub subfield. Repulsion can increase the robustness of the system—to ensure correct wiring even when attraction is disrupted.

Interestingly, when Ten3+ axons simultaneously encounter the Ten3$^+$ and Lphn2$^+$ target subfields, as is the case for the dSub→lat-mMN connection (**Figure 1F, right**; **Figure S1F, G**), conditional target deletion of *Lphn2* alone caused a robust mistargeting phenotype of Ten3$^+$ dSub axons entering the Lphn2$^+$ med-mMN subfield (**Figure 5I**). This indicates that Ten3–Ten3 attraction cannot compensate for the loss of Lphn2–Ten3 repulsion and highlights the importance of simultaneous push and pull in ensuring the correct axon sorting at the choice point. Altogether, these comparative analyses highlight the variations on the basic theme of cooperation between attraction and repulsion during target selection.

Incidentally, the order in which axons encounter the attractant versus repellent subfields also appears to influence the severity of mistargeting when it occurs. In *Ten3* and *Lphn2* double conditional target knockout, the MEC→dSub axons mistarget only to adjacent Lphn2-high regions (**Figure 3**), whereas dSub→lat-mMN axons can mistarget to the most medial region of med-mMN (**Figure S5**). Together, these data indicate the order in which axons encounter attractant and repellent subfields in the target is an important factor to consider in developmental studies.

Multi-functionality and repeated use highlight the economy of wiring molecules

Our study highlights two mechanisms that enable the developing brain to use a limited number of cell-surface recognition proteins to wire up many orders of magnitude more neurons and connections. First, wiring molecules appear to be highly multifunctional, with both Ten3 and Lphn2 serving as both ligand and receptor. Even within the same neuron, Ten3 can simultaneously mediate both attraction and repulsion depending on its interacting partners. For example, in dSub neurons, Ten3 acts cell non-autonomously as an attractive ligand for MEC axons (**Figure 3**) and pCA1 axons,[8] and as a repulsive ligand for dCA1 axons[9] and likely Lphn2$^+$ LEC axons (although this has not been directly tested). At the same time, it acts cell autonomously as a receptor for the Lphn2 repellent in mMN as dSub axons select the appropriate subfield to make connections (**Figure 4**).

Similarly, Lphn2 in pSub neurons acts cell non-autonomously as a repulsive ligand for pCA1 axons[9] as well as for MEC axons (**Figure 3**), while acting cell autonomously as a receptor for target selection in mMN (**Figure 6**). Such multifunctionality is both a result of the molecular property of Ten3 and Lphn2 proteins as a ligand–receptor pair (**Figure 7J**), as well as the circuit architecture of the extended hippocampal network, featuring convergent, divergent, and recurrent connectivity motifs (**Figure 1A$_2$**).[46] Given the prevalence of these connectivity motifs in the mammalian central nervous system, we envision that such multifunctionality of wiring molecules will become a theme when detailed functional analyses are carried out on other molecules and in other circuits. Beyond instructing target selection, members of the teneurin and latrophilin families have been shown to regulate synapse formation in later stages of development within these same regions, highlighting even more roles for these proteins.[38,47,48]

Second, the same molecular module—Ten3–Ten3-mediated attraction and Ten3–Lphn2-mediated mutual repulsions (**Figure 7J**)—appears to be repeatedly used across multiple nodes of the same circuit and potentially many circuits across the brain. We have used systematic conditional knockouts to demonstrate conclusively the repeated use of this molecular module in instructing hard-wired connections in the extended hippocampal network. Our companion manuscripts reported the broad deployment of inverse expression of Ten3 and Lphn2 across many circuits in the mouse brain and the spinal cord.[37,49] In all tested cases, Ten3–Lphn2 inverse expression patterns lay out a topographic map in the developing brain prior to the establishment of functional connections. Importantly, to ensure Ten3$^+$/Lphn2$^+$ neurons from one node do not encounter Ten3$^+$/Lphn2$^+$ neurons from another circuit to produce unintended cross interactions, exquisite spatiotemporal control of their expression and the collaboration with other guidance molecules is likely necessary.

An outstanding question for future research is how the inverse expression patterns of Ten3 and Lphn2 are established during development. Are there shared transcriptional regulatory mechanisms across different brain regions, or do these mechanisms differ region by region? Additionally, other connections within the extended hippocampal network are topographic with inverse expression, including CA1→entorhinal cortex,

subiculum→entorhinal cortex, subiculum →anteroventral thalamus, and mMN→anteroventral thalamus (**Figure 1A$_2$**),[27,31,33,50–53] making it an ideal place to test target selection mechanisms that underlie reciprocal and recurrent connections. Finally, although we know that Lphn2 in lateral hippocampal network is repelled by Ten3 in medial hippocampal network, it has no homophilic binding properties.[9,45] Are there yet-to-be-identified heterophilic attractive partners for Lphn2$^+$ neurons, which will make the Ten3–Lphn2 molecular module more symmetrical? On the other hand, compared to the well investigated ephrin–Eph system, which predominantly operates through reciprocal repulsion,[19,54] the added Ten3–Ten3 homophilic attraction can increase the robustness of this molecular module, potentially contributing to its wide deployment[37,49] beyond the extended hippocampal network investigated here.

Limitations of the study

Although variations in the order of axons encountering attractant versus repellent subfields in the target is the simplest hypothesis to explain why the contribution of repulsion in the targets differs, the evidence available in this study is indirect. Time-lapse imaging studies are needed to confirm axon behavior when encountering the attractant or repellent first. Another limitation is that the loss-of-function experiments use bulk tracing in adult animals. This may reduce the sensitivity to minor mistargeting events either because they have a small magnitude relative to correctly targeted axons or because of correction by developmental or activity-dependent pruning mechanisms. Finally, the use of pan-target Cre drivers reduces our sensitivity to loss-of-attraction phenotypes. Loss of innervation is more apparent with local deletion of Ten3 in the target (via Cre injections)[8] that preserve neighboring expression in the correct subfield as an internal control. Target selection at subiculum and mMN around P0 precludes the use of Cre injection-mediated local deletion.

ACKNOWLEDGEMENTS

We thank the Neuroscience Gene Vector and Virus Core at Stanford University and SignaGen for producing and packaging custom viruses, T. Südhof for the *Lphn2^{mVenus}* and *Lphn2^{floxed}* mice, and members of the Luo lab, especially U. Chon, for advice and support. We thank T. Hindmarsh-Sten, A. Starr, Z. Li, K. Sangster, and A. Kania for critiques of the manuscript. E.C.G. was supported by National Institute of Mental Health, Ruth L. Kirschstein National Research Service Award (F31MH129079). D.T.P. was supported by an American Australian Association Education Fund Scholarship and the SFARI Fellows-to-Faculty Award (Simons Foundation). L.L. is an investigator at Howard Hughes Medical Institute. This work was supported by National Institutes of Health grant (R01-NS050580 to L.L.).

AUTHOR CONTRIBUTIONS

E.C.G. and D.T.P. conceptualized the study. E.C.G. performed all the experiments, except for the RNAscope assay, which was performed by Y.Z. E.C.G. analyzed all data and wrote the manuscript. L.L. supervised the study and edited the manuscript.

DECLARATION OF INTERESTS

L.L. is a member of the advisory board of *Cell*.

REFERENCES

1. Sperry, R.W. (1963). Chemoaffinity in the orderly growth of nerve fiber patterns and connections*. Proc. Natl. Acad. Sci. *50*, 703–710. https://doi.org/10.1073/pnas.50.4.703.
2. Sanes, J.R., and Zipursky, S.L. (2020). Synaptic Specificity, Recognition Molecules, and Assembly of Neural Circuits. Cell *181*, 536–556. https://doi.org/10.1016/j.cell.2020.04.008.
3. Kolodkin, A.L., and Tessier-Lavigne, M. (2011). Mechanisms and Molecules of Neuronal Wiring: A Primer. Cold Spring Harb. Perspect. Biol. *3*, a001727. https://doi.org/10.1101/cshperspect.a001727.
4. Walter, J., Kern-Veits, B., Huf, J., Stolze, B., and Bonhoeffer, F. (1987). Recognition of position-specific properties of tectal cell membranes by retinal axons in vitro. Development *101*, 685–696.
5. Cheng, H.-J., Nakamoto, M., Bergemann, A.D., and Flanagan, J.G. (1995). Complementary gradients in expression and binding of ELF-1 and Mek4 in development of the topographic retinotectal projection map. Cell *82*, 371–381. https://doi.org/10.1016/0092-8674(95)90426-3.
6. Drescher, U., Kremoser, C., Handwerker, C., Löschinger, J., Noda, M., and Bonhoeffer, F. (1995). In vitro guidance of retinal ganglion cell axons by RAGS, a 25 kDa tectal protein related to ligands for Eph receptor tyrosine kinases. Cell *82*, 359–370. https://doi.org/10.1016/0092-8674(95)90425-5.
7. Hong, W., Mosca, T.J., and Luo, L. (2012). Teneurins instruct synaptic partner matching in an olfactory map. Nature *484*, 201–207. https://doi.org/10.1038/nature10926.
8. Berns, D.S., DeNardo, L.A., Pederick, D.T., and Luo, L. (2018). Teneurin-3 controls topographic circuit assembly in the hippocampus. Nature *554*, 328–333. https://doi.org/10.1038/nature25463.
9. Pederick, D.T., Lui, J.H., Gingrich, E.C., Xu, C., Wagner, M.J., Liu, Y., He, Z., Quake, S.R., and Luo, L. (2021). Reciprocal repulsions instruct the precise assembly of parallel hippocampal networks. Science *372*, 1068–1073. https://doi.org/10.1126/science.abg1774.
10. Duan, X., Krishnaswamy, A., Laboulaye, M.A., Liu, J., Peng, Y.-R., Yamagata, M., Toma, K., and Sanes, J.R. (2018). Cadherin Combinations Recruit Dendrites of Distinct Retinal Neurons to a Shared Interneuronal Scaffold. Neuron *99*, 1145-1154.e6. https://doi.org/10.1016/j.neuron.2018.08.019.
11. Dombrovski, M., Zang, Y., Frighetto, G., Vaccari, A., Jang, H., Mirshahidi, P.S., Xie, F., Sanfilippo, P., Hina, B.W., Rehan, A., et al. (2025). Molecular gradients shape synaptic specificity of a visuomotor transformation. Nature *644*, 453–462. https://doi.org/10.1038/s41586-025-09037-4.
12. Li, Z., Lyu, C., Xu, C., Hu, Y., Luginbuhl, D.J., Caspi-Lebovic, A.B., Priest, J.M., Özkan, E., and Luo, L. (2025). Repulsive interactions instruct synaptic partner matching in an olfactory circuit. Preprint at bioRxiv, https://doi.org/10.1101/2025.03.01.640985.
13. Lyu, C., Li, Z., Xu, C., Kalai, J., and Luo, L. (2025). Rewiring an olfactory circuit by altering the combinatorial code of cell-surface proteins. Preprint at bioRxiv, https://doi.org/10.1101/2025.03.01.640986.
14. Azevedo, F.A.C., Carvalho, L.R.B., Grinberg, L.T., Farfel, J.M., Ferretti, R.E.L., Leite, R.E.P., Jacob Filho, W., Lent, R., and Herculano-Houzel, S. (2009). Equal numbers of neuronal and nonneuronal cells make the human brain an isometrically scaled-up primate brain. J. Comp. Neurol. *513*, 532–541. https://doi.org/10.1002/cne.21974.
15. Andrade-Moraes, C.H., Oliveira-Pinto, A.V., Castro-Fonseca, E., da Silva, C.G., Guimarães, D.M., Szczupak, D., Parente-Bruno, D.R., Carvalho, L.R.B., Polichiso, L., Gomes, B.V., et al. (2013). Cell number changes in Alzheimer's disease relate to dementia, not to plaques and tangles. Brain J. Neurol. *136*, 3738–3752. https://doi.org/10.1093/brain/awt273.
16. Goriely, A. (2025). Eighty-six billion and counting: do we know the number of neurons in the human brain? Brain *148*, 689–691. https://doi.org/10.1093/brain/awae390.
17. Bausch-Fluck, D., Goldmann, U., Müller, S., van Oostrum, M., Müller, M., Schubert, O.T., and Wollscheid, B. (2018). The in silico human surfaceome. Proc. Natl. Acad. Sci. *115*, E10988–E10997. https://doi.org/10.1073/pnas.1808790115.
18. Luo, L. (2021). Principles of Neurobiology 2nd ed. (CRC Press).
19. Cang, J., and Feldheim, D.A. (2013). Developmental Mechanisms of Topographic Map Formation and Alignment. Annu. Rev. Neurosci. *36*, 51–77. https://doi.org/10.1146/annurev-neuro-062012-170341.

20. Brown, A., Yates, P.A., Burrola, P., Ortuño, D., Vaidya, A., Jessell, T.M., Pfaff, S.L., O'Leary, D.D.M., and Lemke, G. (2000). Topographic Mapping from the Retina to the Midbrain Is Controlled by Relative but Not Absolute Levels of EphA Receptor Signaling. Cell *102*, 77–88. https://doi.org/10.1016/S0092-8674(00)00012-X.
21. Feldheim, D.A., Kim, Y.-I., Bergemann, A.D., Frisén, J., Barbacid, M., and Flanagan, J.G. (2000). Genetic Analysis of Ephrin-A2 and Ephrin-A5 Shows Their Requirement in Multiple Aspects of Retinocollicular Mapping. Neuron *25*, 563–574. https://doi.org/10.1016/S0896-6273(00)81060-0.
22. Rashid, T., Upton, A.L., Blentic, A., Ciossek, T., Knöll, B., Thompson, I.D., and Drescher, U. (2005). Opposing Gradients of Ephrin-As and EphA7 in the Superior Colliculus Are Essential for Topographic Mapping in the Mammalian Visual System. Neuron *47*, 57–69. https://doi.org/10.1016/j.neuron.2005.05.030.
23. Triplett, J.W., Owens, M.T., Yamada, J., Lemke, G., Cang, J., Stryker, M.P., and Feldheim, D.A. (2009). Retinal input instructs alignment of visual topographic maps. Cell *139*, 175–185. https://doi.org/10.1016/j.cell.2009.08.028.
24. Suetterlin, P., and Drescher, U. (2014). Target-Independent EphrinA/EphA-Mediated Axon-Axon Repulsion as a Novel Element in Retinocollicular Mapping. Neuron *84*, 740–752. https://doi.org/10.1016/j.neuron.2014.09.023.
25. Igarashi, K.M., Ito, H.T., Moser, E.I., and Moser, M.-B. (2014). Functional diversity along the transverse axis of hippocampal area CA1. FEBS Lett. *588*, 2470–2476. https://doi.org/10.1016/j.febslet.2014.06.004.
26. Cembrowski, M.S., Phillips, M.G., DiLisio, S.F., Shields, B.C., Winnubst, J., Chandrashekar, J., Bas, E., and Spruston, N. (2018). Dissociable Structural and Functional Hippocampal Outputs via Distinct Subiculum Cell Classes. Cell *173*, 1280-1292.e18. https://doi.org/10.1016/j.cell.2018.03.031.
27. Tamamaki, N., and Nojyo, Y. (1995). Preservation of topography in the connections between the subiculum, field CA1, and the entorhinal cortex in rats. J. Comp. Neurol. *353*, 379–390. https://doi.org/10.1002/cne.903530306.
28. Allen, G.V., and Hopkins, D.A. (1989). Mamillary body in the rat: topography and synaptology of projections from the subicular complex, prefrontal cortex, and midbrain tegmentum. J. Comp. Neurol. *286*, 311–336. https://doi.org/10.1002/cne.902860303.
29. Shibata, H. (1989). Descending projections to the mammillary nuclei in the rat, as studied by retrograde and anterograde transport of wheat germ agglutinin-horseradish peroxidase. J. Comp. Neurol. *285*, 436–452. https://doi.org/10.1002/cne.902850403.
30. Kishi, T., Tsumori, T., Ono, K., Yokota, S., Ishino, H., and Yasui, Y. (2000). Topographical organization of projections from the subiculum to the hypothalamus in the rat. J. Comp. Neurol. *419*, 205–222. https://doi.org/10.1002/(SICI)1096-9861(20000403)419:2%253C205::AID-CNE5%253E3.0.CO;2-0.
31. Naber, P.A., Lopes da Silva, F.H., and Witter, M.P. (2001). Reciprocal connections between the entorhinal cortex and hippocampal fields CA1 and the subiculum are in register with the projections from CA1 to the subiculum. Hippocampus *11*, 99–104. https://doi.org/10.1002/hipo.1028.
32. van Strien, N.M., Cappaert, N.L.M., and Witter, M.P. (2009). The anatomy of memory: an interactive overview of the parahippocampal–hippocampal network. Nat. Rev. Neurosci. *10*, 272–282. https://doi.org/10.1038/nrn2614.
33. Wright, N.F., Erichsen, J.T., Vann, S.D., O'Mara, S.M., and Aggleton, J.P. (2010). Parallel but separate inputs from limbic cortices to the mammillary bodies and anterior thalamic nuclei in the rat. J. Comp. Neurol. *518*, 2334–2354. https://doi.org/10.1002/cne.22336.
34. Pederick, D.T., Perry-Hauser, N.A., Meng, H., He, Z., Javitch, J.A., and Luo, L. (2023). Context-dependent requirement of G protein coupling for Latrophilin-2 in target selection of hippocampal axons. eLife *12*, e83529. https://doi.org/10.7554/eLife.83529.
35. Donohue, J.D., Amidon, R.F., Murphy, T.R., Wong, A.J., Liu, E.D., Saab, L., King, A.J., Pae, H., Ajayi, M.T., and Anderson, G.R. (2021). Parahippocampal latrophilin-2 (ADGRL2) expression controls topographical presubiculum to entorhinal cortex circuit connectivity. Cell Rep. *37*, 110031. https://doi.org/10.1016/j.celrep.2021.110031.

36. Liakath-Ali, K., Refaee, R., and Südhof, T.C. (2024). Cartography of teneurin and latrophilin expression reveals spatiotemporal axis heterogeneity in the mouse hippocampus during development. PLOS Biol. *22*, e3002599. https://doi.org/10.1371/journal.pbio.3002599.
37. Chon, U., Pederick, D.T., Song, J.H., Zhang, Y., Rana, I., and Luo, L. (2025). Inverse expression of Ten3 and Lphn2 across the developing mouse brain reveals a global strategy for circuit assembly. Preprint at bioRxiv, https://doi.org/10.1101/2025.08.13.670004.
38. Anderson, G.R., Maxeiner, S., Sando, R., Tsetsenis, T., Malenka, R.C., and Südhof, T.C. (2017). Postsynaptic adhesion GPCR latrophilin-2 mediates target recognition in entorhinal-hippocampal synapse assembly. J. Cell Biol. *216*, 3831–3846. https://doi.org/10.1083/jcb.201703042.
39. Wang, F., Flanagan, J., Su, N., Wang, L.-C., Bui, S., Nielson, A., Wu, X., Vo, H.-T., Ma, X.-J., and Luo, Y. (2012). RNAscope: A Novel in Situ RNA Analysis Platform for Formalin-Fixed, Paraffin-Embedded Tissues. J. Mol. Diagn. *14*, 22–29. https://doi.org/10.1016/j.jmoldx.2011.08.002.
40. The MouseLight Project (Howard Hughes Medical Institute, Janelia Campus).
41. Digital Brain - Projectome Atlas (Institute of Neuroscience, Chinese Academy of Sciences).
42. Qiu, S., Hu, Y., Huang, Y., Gao, T., Wang, X., Wang, D., Ren, B., Shi, X., Chen, Y., Wang, X., et al. (2024). Whole-brain spatial organization of hippocampal single-neuron projectomes. Science *383*, eadj9198. https://doi.org/10.1126/science.adj9198.
43. Winnubst, J., Bas, E., Ferreira, T.A., Wu, Z., Economo, M.N., Edson, P., Arthur, B.J., Bruns, C., Rokicki, K., Schauder, D., et al. (2019). Reconstruction of 1,000 Projection Neurons Reveals New Cell Types and Organization of Long-Range Connectivity in the Mouse Brain. Cell *179*, 268-281.e13. https://doi.org/10.1016/j.cell.2019.07.042.
44. Economo, M.N., Clack, N.G., Lavis, L.D., Gerfen, C.R., Svoboda, K., Myers, E.W., and Chandrashekar, J. (2016). A platform for brain-wide imaging and reconstruction of individual neurons. eLife *5*, e10566. https://doi.org/10.7554/eLife.10566.
45. Boucard, A.A., Maxeiner, S., and Südhof, T.C. (2014). Latrophilins Function as Heterophilic Cell-adhesion Molecules by Binding to Teneurins: REGULATION BY ALTERNATIVE SPLICING*. J. Biol. Chem. *289*, 387–402. https://doi.org/10.1074/jbc.M113.504779.
46. Luo, L. (2021). Architectures of neuronal circuits. Science *373*, eabg7285. https://doi.org/10.1126/science.abg7285.
47. Sando, R., Jiang, X., and Südhof, T.C. (2019). Latrophilin GPCRs direct synapse specificity by coincident binding of FLRTs and teneurins. Science *363*, eaav7969. https://doi.org/10.1126/science.aav7969.
48. Sando, R., and Südhof, T.C. (2021). Latrophilin GPCR signaling mediates synapse formation. eLife *10*, e65717. https://doi.org/10.7554/eLife.65717.
49. Sangster, K.T., Zhang, X., Toro, D. del, Sarantopoulos, C., Moses, A.M., Mahasenan, S., Pederick, D.T., Roome, R.B., Seiradake, E., Luo, L., et al. (2025). Teneurin-3 and Latrophilin-2 are required for the formation of a somatotopic map and somatosensory topognosis. Preprint at bioRxiv, https://doi.org/10.1101/2025.08.13.670179.
50. Wright, N.F., Vann, S.D., Erichsen, J.T., O'Mara, S.M., and Aggleton, J.P. (2013). Segregation of parallel inputs to the anteromedial and anteroventral thalamic nuclei of the rat. J. Comp. Neurol. *521*, 2966–2986. https://doi.org/10.1002/cne.23325.
51. Seki, M., and Zyo, K. (1984). Anterior thalamic afferents from the mamillary body and the limbic cortex in the rat. J. Comp. Neurol. *229*, 242–256. https://doi.org/10.1002/cne.902290209.
52. Hayakawa, T., and Zyo, K. (1989). Retrograde double-labeling study of the marnmillothalamic and the mammillotegmental projections in the rat. J. Comp. Neurol. *284*, 1–11. https://doi.org/10.1002/cne.902840102.
53. Shibata, H. (1992). Topographic organization of subcortical projections to the anterior thalamic nuclei in the rat. J. Comp. Neurol. *323*, 117–127. https://doi.org/10.1002/cne.903230110.
54. Egea, J., and Klein, R. (2007). Bidirectional Eph–ephrin signaling during axon guidance. Trends Cell Biol. *17*, 230–238. https://doi.org/10.1016/j.tcb.2007.03.004.

55. Fenno, L.E., Mattis, J., Ramakrishnan, C., Hyun, M., Lee, S.Y., He, M., Tucciarone, J., Selimbeyoglu, A., Berndt, A., Grosenick, L., et al. (2014). Targeting cells with single vectors using multiple-feature Boolean logic. Nat. Methods *11*, 763–772. https://doi.org/10.1038/nmeth.2996.
56. Saunders, A., Johnson, C., and Sabatini, B. (2012). Novel recombinant adeno-associated viruses for Cre activated and inactivated transgene expression in neurons. Front. Neural Circuits *6*. https://doi.org/10.3389/fncir.2012.00047.
57. Boyden, E.S., Zhang, F., Bamberg, E., Nagel, G., and Deisseroth, K. (2005). Millisecond-timescale, genetically targeted optical control of neural activity. Nat. Neurosci. *8*, 1263–1268. https://doi.org/10.1038/nn1525.
58. Leinninger, G.M., Opland, D.M., Jo, Y.-H., Faouzi, M., Christensen, L., Cappellucci, L.A., Rhodes, C.J., Gnegy, M.E., Becker, J.B., Pothos, E.N., et al. (2011). Leptin Action via Neurotensin Neurons Controls Orexin, the Mesolimbic Dopamine System and Energy Balance. Cell Metab. *14*, 313–323. https://doi.org/10.1016/j.cmet.2011.06.016.
59. Balthasar, N., Dalgaard, L.T., Lee, C.E., Yu, J., Funahashi, H., Williams, T., Ferreira, M., Tang, V., McGovern, R.A., Kenny, C.D., et al. (2005). Divergence of Melanocortin Pathways in the Control of Food Intake and Energy Expenditure. Cell *123*, 493–505. https://doi.org/10.1016/j.cell.2005.08.035.
60. Quina, L.A., Harris, J., Zeng, H., and Turner, E.E. (2017). Specific connections of the interpeduncular subnuclei reveal distinct components of the habenulopeduncular pathway. J. Comp. Neurol. *525*, 2632–2656. https://doi.org/10.1002/cne.24221.

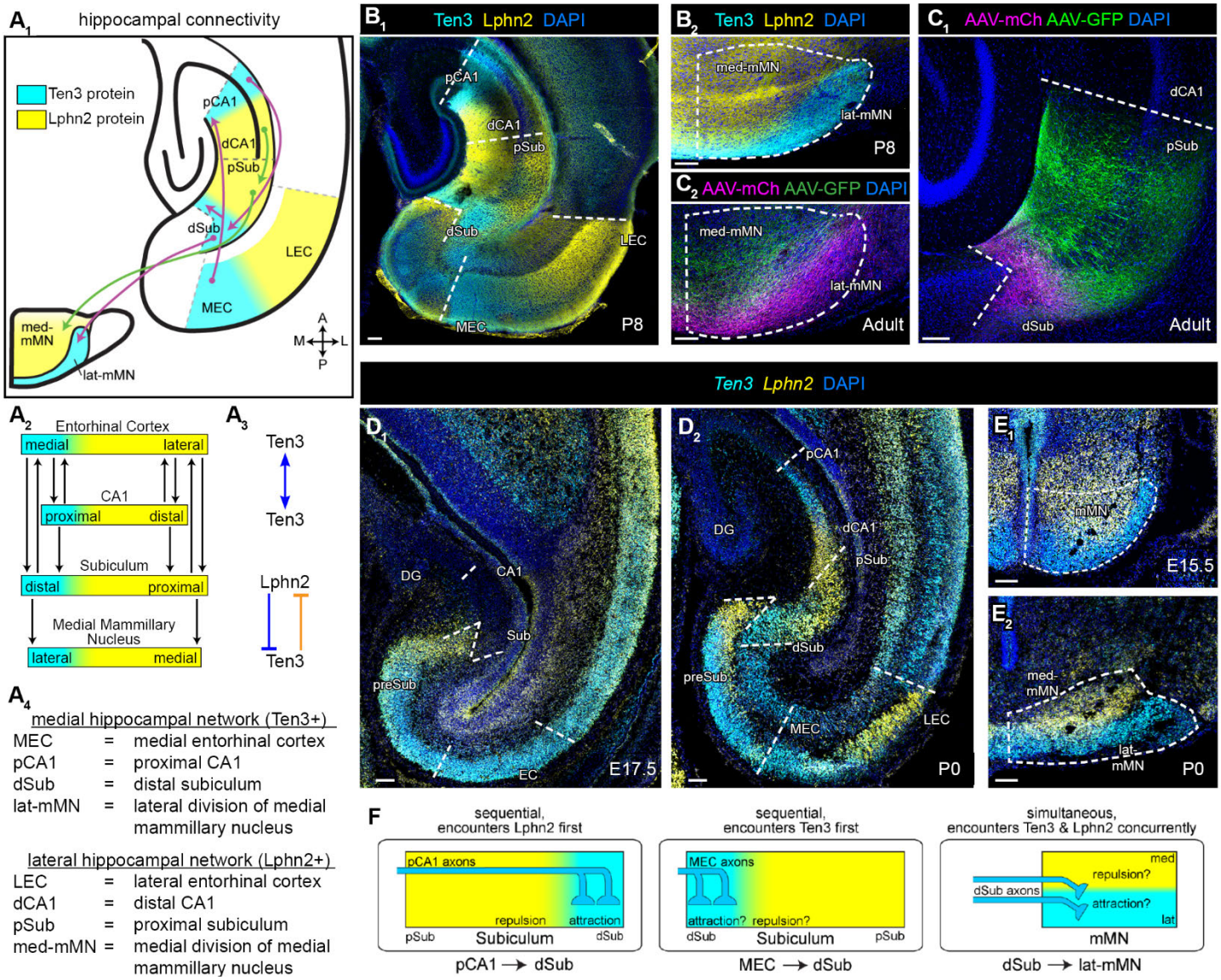

Figure 1. Inverse Ten3 and Lphn2 expression patterns match the topography of the extended hippocampal network during development.

(A) Overview. (A_1) Summary of topographic connectivity addressed in this study, overlaid on P8 Ten3 and Lphn2 protein expression. (A_2) All connectivity between four different nodes of the medial and lateral hippocampal network. (A_3) Summary of molecular interactions between Ten3 and Lphn2. The bidirectional arrow represents attraction; —| represents repulsion from target to axon. Blue mechanisms are used for $Ten3^+$ axons, whereas the orange mechanism is used for $Lphn2^+$ axons. (A_4) Anatomical abbreviations.

(B) Inverse protein expression of Ten3 and Lphn2 in hippocampus and entorhinal cortex (B_1) and medial mammillary nucleus (mMN) of the hypothalamus (B_2) of P8 $Ten3^{HA/HA}$;$Lphn2^{mVenus/mVenus}$ mouse.

(C) Dual anterograde tracer injections into neighboring sites in distal subiculum (dSub) and proximal subiculum (pSub; C_1) result in topographic projections to neighboring sites in lateral (lat-mMN) and medial (med-mMN) mMN, respectively (C_2).

(D) mRNA expression of *Ten3* (cyan) and *Lphn2* (yellow) at E17.5 (D_1) and P0 (D_2) in hippocampus and entorhinal cortex. At E17.5, only *Ten3* mRNA is detectable in EC. By P0, CA1, Sub, and EC all have inverse mRNA expression of *Ten3* and *Lphn2*.

(E) mRNA expression of *Ten3* (cyan) and *Lphn2* (yellow) at E15.5 (E_1) and P0 (E_2) in mMN.

(F) Summary of three different axon entry routes with respect to Ten3 and Lphn2 expression subfields in target. Scale bars, 100 µm. See Figure S1 for additional data. See Table S1 for detailed genotypes.

In this and all subsequent figures, A, anterior; P, posterior; M, medial; L, lateral.

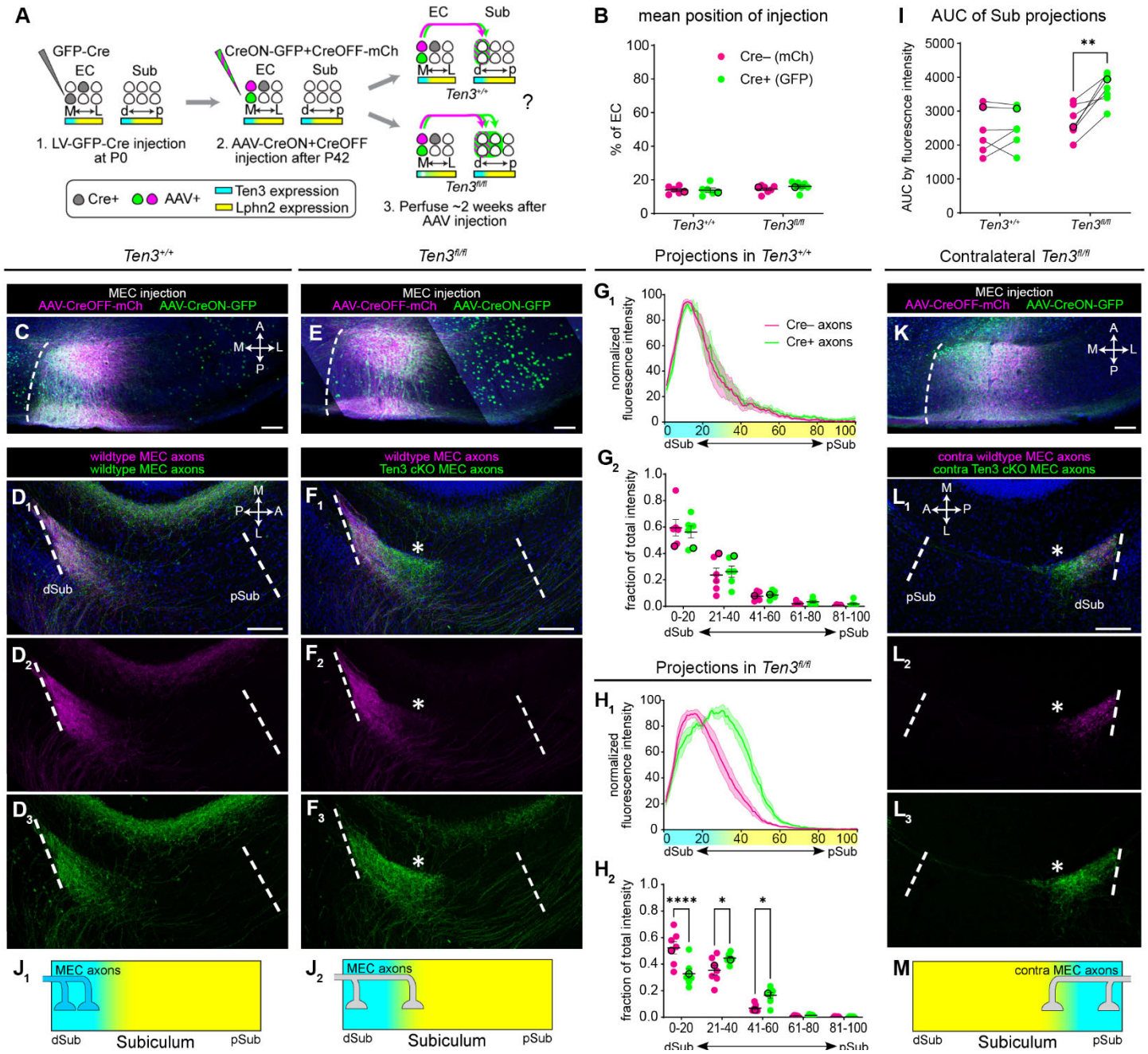

Figure 2. Ten3 is required in medial entorhinal cortex axons for their precise targeting to distal subiculum
(A) Injection strategy and possible results for tracing MEC axons into subiculum of control (top right) and *Ten3*$^{fl/fl}$ mice (bottom right; white dot in cyan area in the bottom designates *Ten3* deletion in a subset of MEC neurons).
(B) Mean positions of injection sites along the medial-to-lateral axis of entorhinal cortex (EC) show no differences between *Ten3*$^{+/+}$ controls (n = 6 mice) and *Ten3*$^{fl/fl}$ mice (n = 7 mice). Black outline indicates representative animals shown in C, E. Mean ± SEM. Mann-Whitney tests corrected for multiple comparisons (Holm-Šídák), no significant differences.
(C) Representative image of the *AAV-CreON/CreOFF* injection site of *Ten3*$^{+/+}$ controls show both viruses restricted to the most medial region of entorhinal cortex. Injection corresponds to animal in D.
(D) Representative images of projection of Cre^{-} axons (magenta) and Cre^{+} axons (green) into molecular layer of subiculum in *Ten3*$^{+/+}$ controls. The three images are from the same confocal section showing merge (D_1), magenta only (D_2), or green only (D_3) channels.

(E, F) Same as C, D but for *Ten3*$^{fl/fl}$ mice. *Ten3*^{MEC}-cKO axons spread beyond the Cre^{-} control axons toward pSub (asterisk in F, in identical position across three images). Green dots in C and E come from *Cre-GFP* lentivirus, rather than *AAV-CreON-GFP*.
(G_1) Normalized fluorescence intensity traces of the Cre^{-} (magenta) and Cre^{+} (green) projections along the distal–proximal axis of subiculum in *Ten3*$^{+/+}$ controls (n = 6 mice). Ten3 (cyan) and Lphn2 (yellow) expression is represented along the x-axis. Mean (dark line) ± SEM (shaded area).
(G_2) Fraction of total projection intensity (same data as G_1) in 20% bins of subiculum axis of the Cre^{-} (magenta) and Cre^{+} (green) projections along the distal–proximal axis of subiculum in *Ten3*$^{+/+}$ controls (n = 6 mice). Black outlines indicate representative animal shown in D. Mean ± SEM. Two-way ANOVA corrected for multiple comparisons (Šídák correction), no significant differences.
(H) Same as G but for *Ten3*$^{fl/fl}$ (n = 7) mice. **** $p < 0.0001$, * $p < 0.05$.
(I) Area under the curve of averaged subiculum projections for *Ten3*$^{+/+}$ controls (n = 6 mice) and *Ten3*$^{fl/fl}$ mice (n = 7 mice). Lines are drawn between Cre^{-} (magenta) and Cre^{+} (green) projections within the same animal. Open circles indicate representative animals shown in D, F. Mann-Whitney tests corrected for multiple comparisons (Holm-Šídák), ** $p < 0.01$.
(J) Schematic summary of target selection of MEC axons in subiculum in control (J_1) and *Ten3*^{MEC}-cKO (J_2) based on results in C–I.
(K, L) Same as E, F, but for projections into contralateral subiculum. Contralateral Cre^{+}, *Ten3*^{MEC}-cKO axons spread beyond the contralateral Cre^{-} control axons toward pSub (asterisk, in identical position across three images).
(M) Schematic summary of target selection of *Ten3*^{MEC}-cKO axons in contralateral subiculum.
Scale bars, 100 μm. See Figure S2 for additional data. See Table S1 for detailed genotypes.

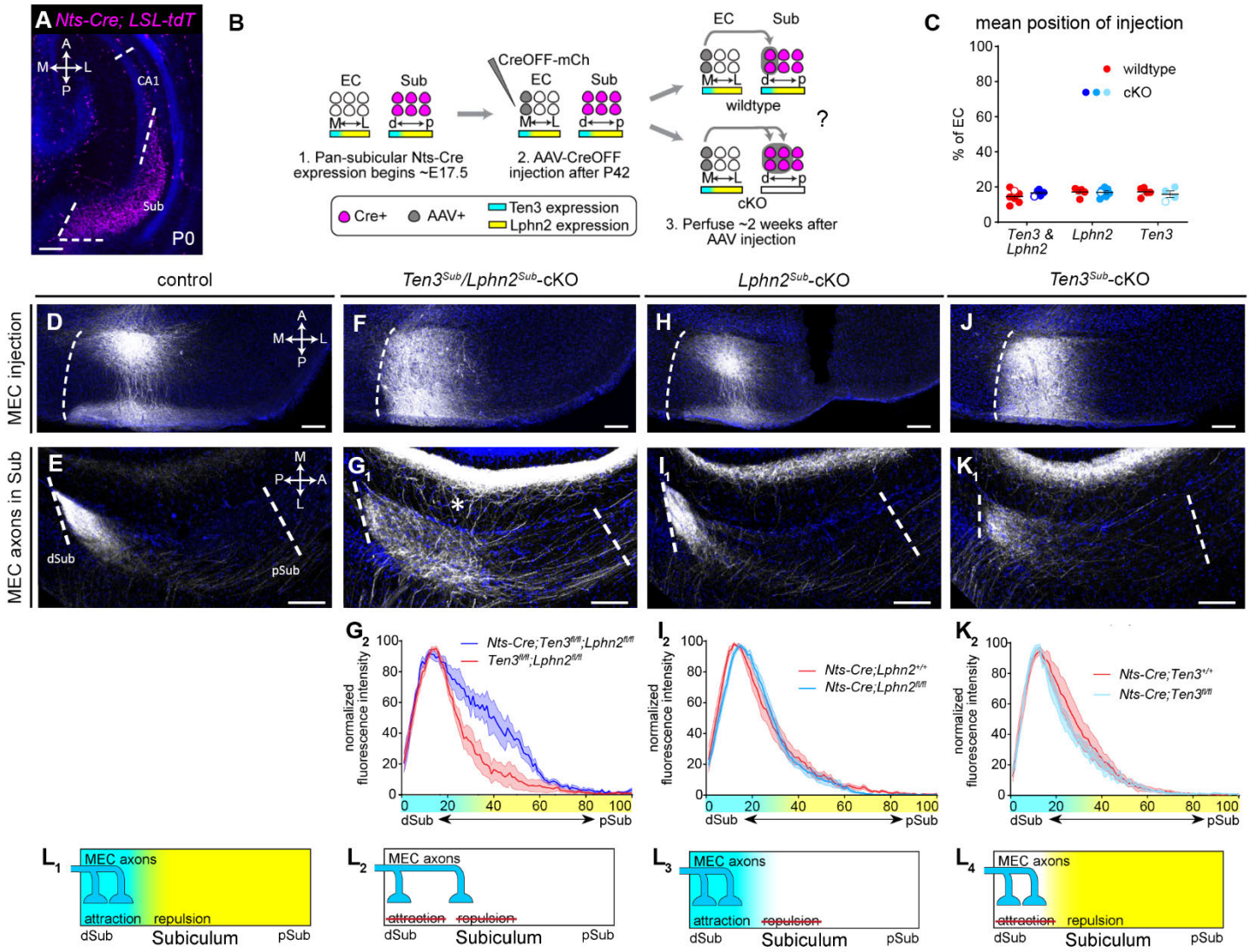

Figure 3. Ten3 and Lphn2 in subiculum cooperate to instruct the precise targeting of medial entorhinal cortex axons

(A) *Nts-Cre* is densely expressed in subiculum at P0, as assessed by a nuclear tdTomato reporter. Scale bar, 150 µm.

(B) Injection strategy and possible results for tracing MEC axons into subiculum of control (top right) and *Ten3^{Sub}/Lphn2^{Sub}*-cKO mice (bottom right).

(C) Mean position of injection sites along the medial-to-lateral axis of entorhinal cortex (EC) show no differences between *Ten3^{Sub}/Lphn2^{Sub}*-cKO (n = 5 mice), *Lphn2^{Sub}*-cKO (n = 7 mice), *Ten3^{Sub}*-cKO (n = 4 mice), and their respective littermate controls (n=5, 5, 4, respectively). Open circles indicate representative animals shown in D, F, H, J. Mean ± SEM. Mann-Whitney tests corrected for multiple comparisons (Holm-Šídák), no significant differences.

(D) Representative image of the *AAV-CreOFF* injection site of *Ten3$^{fl/fl}$;Lphn2$^{fl/fl}$* controls shows that virus is restricted to the most medial region of entorhinal cortex. Injection corresponds to animal in E. Scale bar, 100 µm.

(E) Representative image of projection into molecular layer of subiculum for *Ten3$^{fl/fl}$;Lphn2$^{fl/fl}$* (control). Scale bar, 100 µm.

(F, H, J) Same as D, but for genotypes indicated above.

(G_1, I_1, K_1) Same as E, but for genotypes indicated above. MEC axons in *Ten3^{Sub}/Lphn2^{Sub}*-cKO mice spread proximally beyond dSub (asterisk in G_1).

(G_2, I_2, K_2) Normalized fluorescence intensity traces in genotypes as indicated. Mean (dark line) ± SEM (shaded area). n = 7, 5 for control and *Ten3*^{Sub}/*Lphn2*^{Sub}-cKO mice, respectively (G_2); n = 5, 7 for control and *Lphn2*^{Sub}-cKO mice, respectively (I_2); n = 5, 4 for control and *Ten3*^{Sub}-cKO mice, respectively (K_2). Ten3 (cyan) and Lphn2 (yellow) expression is represented along the x-axis. Mean (dark line) ± SEM (shaded area).
(L) Schematic summary of target selection of MEC axons in subiculum when *Ten3* (L_4), *Lphn2* (L_3), or both (L_2) were conditionally knocked out in subiculum target.
See Figure S3–S4 for additional data. See Table S1 for detailed genotypes.

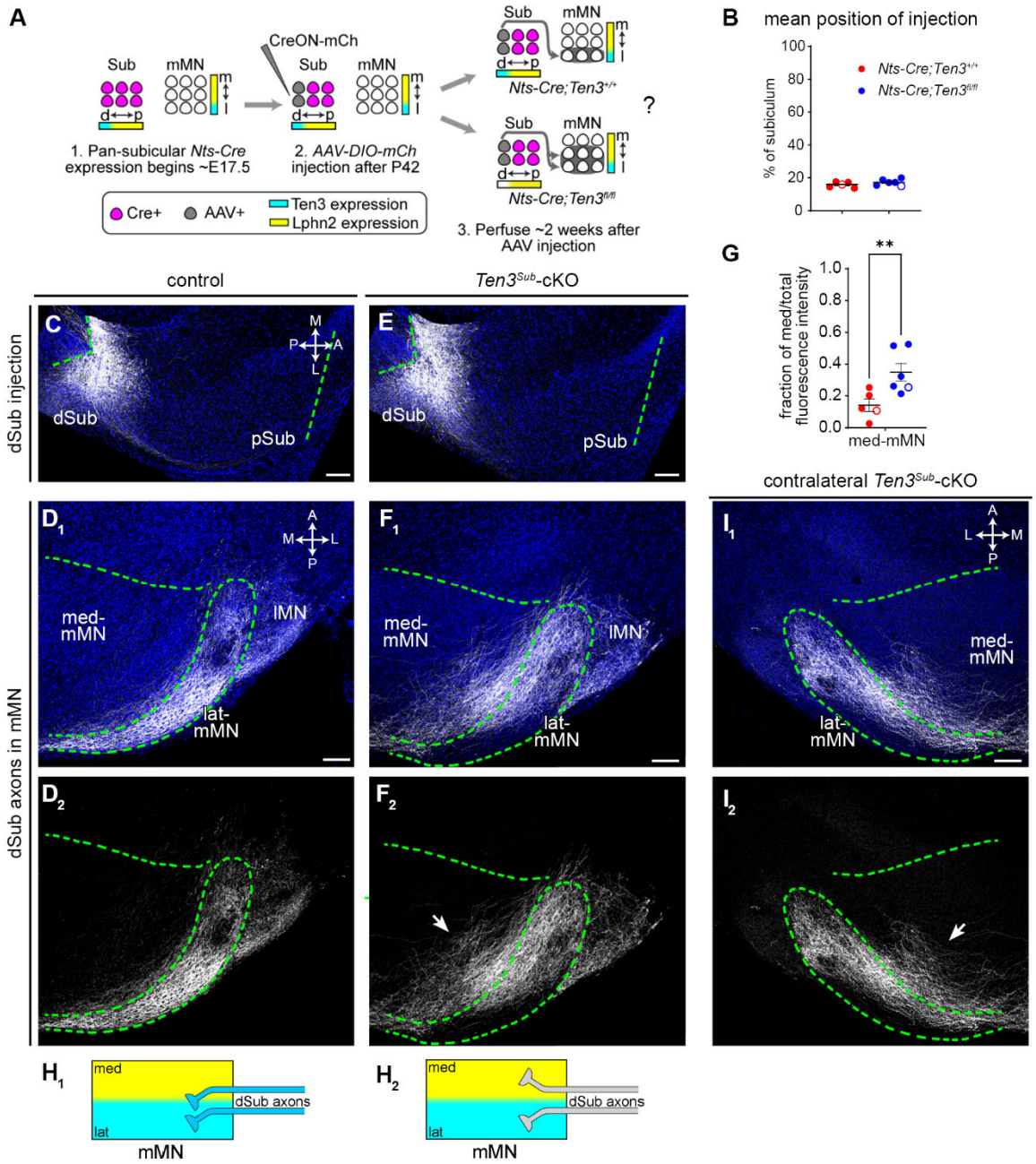

Figure 4. Ten3 is required in subiculum for dSub axons to precisely targeting to lateral mMN

(A) Injection strategy and possible results for tracing dSub axons into medial mammillary nucleus (mMN) of control (top right) and *Ten3*^{Sub}-cKO mice (bottom right).

(B) Mean positions of injection sites along the distal-to-proximal axis of subiculum show no differences between controls (n = 5 mice) and *Ten3*^{Sub}-cKO (n = 6 mice). Open circles indicate representative animals shown in C, E. Mean ± SEM. Mann-Whitney test, no significant differences.

(C) Representative image of the *AAV-mCh* (gray) injection site of controls show that the virus is restricted to the most distal region of subiculum. Injection corresponds to animal in D.

(D) Representative images of projection of dSub axons (gray) into mMN of controls (D_1). Bottom panel shows axons without DAPI counterstain (D_2). Labeling in the lateral mammillary nucleus (lMN) are unrelated axons from pre-subiculum.

(E, F) Same as C, D, but for *Ten3*^{Sub}-cKO mice. *Ten3*^{Sub}-cKO axons spread into the med-mMN (arrow).

(G) Fraction of total projection intensity of the dSub axons in med-mMN in controls (red) and *Ten3*^{Sub}-cKO (blue). Open circles indicate representative animals shown in D, F. Mean ± SEM. Mann-Whitney test, ** $p < 0.01$.

(H) Schematic summary of target selection of dSub axons in mMN of control (H_1) and *Ten3*^{Sub}-cKO (H_2) mice based on results in C–G.
(I) Same as F, but for projections into contralateral mMN. Contralateral *Ten3*^{Sub}-cKO axons spread into the med-mMN (arrow).
Scale bars, 100 μm. Anatomical borders were drawn based on DAPI counterstain (Figure S5H).
See Figure S3 and S5 for additional data. See Table S1 for detailed genotypes.

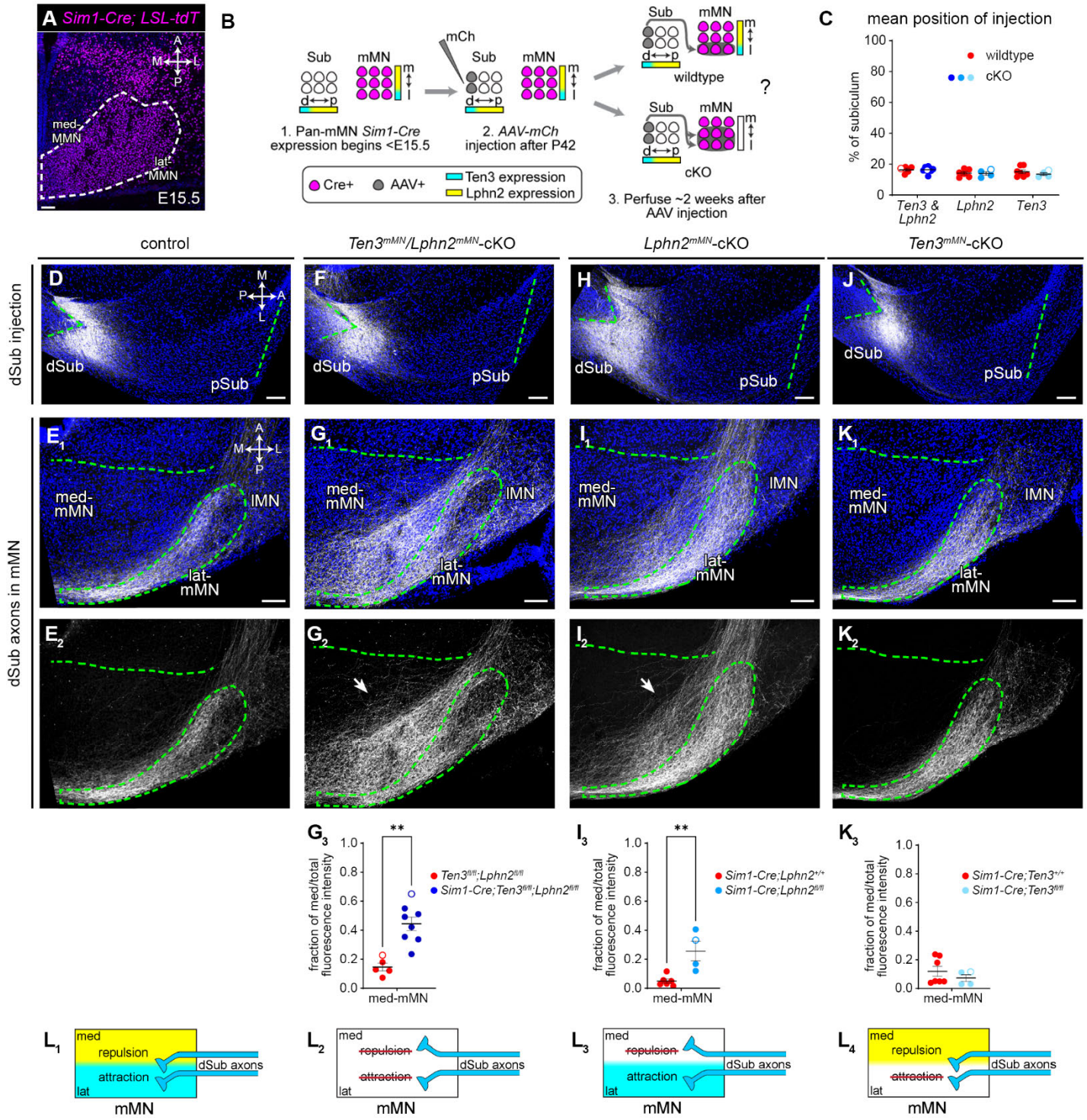

Figure 5. Lphn2 is required in mMN for the precise targeting of dSub axons to lat-mMN

(A) *Sim1-Cre* is densely expressed in mMN by E15.5, as assessed by a nuclear tdTomato reporter. Scale bar, 50 µm.

(B) Injection strategy and possible results for tracing dSub axons into medial mammillary nucleus (mMN) of controls (top right) and *Ten3*^{mMN}/*Lphn2*^{mMN}-cKO mice (bottom right).

(C) Mean positions of injection sites along the distal-to-proximal axis of subiculum show no differences between *Ten3*^{mMN}/*Lphn2*^{mMN}-cKO (left; n=8), *Lphn2*^{mMN}-cKO (middle; n=4), *and Ten3*^{mMN}-cKO (right; n=4), and their respective littermate controls (n=5, 6, 7, respectively). Open circles indicate representative animals shown in D,

F, H, J. Mean ± SEM. Mann-Whitney tests corrected for multiple comparisons (Holm-Šídák), no significant differences.
(D) Representative image of the *AAV-mCh* (gray) injection site of controls show that the virus is restricted to the most distal region of subiculum. Injection corresponds to animal in E. Scale bar, 100 µm.
(E) Representative images of projection into mMN of control mice (E_1). Bottom panel shows axons without DAPI counterstain (E_2). Labeling in lMN are unrelated axons from pre-subiculum. Scale bar, 100 µm.
(F, H, J) Same as D, but for genotypes indicated above.
($G_{1,2}$, $I_{1,2}$, $K_{1,2}$) Same as E, but for genotypes indicated above. dSub axons in *Ten3*^{mMN}/*Lphn2*^{mMN}-cKO (G) and *Lphn2*^{mMN}-cKO (I) mice spread medially outside of lat-mMN (arrows in G_2, I_2).
(G_3, I_3, K_3) Fraction of total projection intensity of the dSub axons in med-mMN for genotypes indicated above. n = 5, 8 for control and *Ten3*^{mMN}/*Lphn2*^{mMN}-cKO mice, respectively (G_2); n = 6, 4 for control and *Lphn2*^{mMN}-cKO mice, respectively (I_2); n = 7, 4 for control and *Ten3*^{mMN}-cKO mice, respectively (K_2). Open circles indicate representative animals shown in E, G, I, K. Mean ± SEM. Mann-Whitney test, ** $p < 0.01$.
(L) Schematic summary of target selection of dSub axons in mMN when *Ten3* (L_4), *Lphn2* (L_3), or both (L_2) were conditionally knocked out in mMN.
Anatomical borders were drawn based on DAPI counterstain (Figure S5H).
See Figure S3 and S6 for additional data. See Table S1 for detailed genotypes.

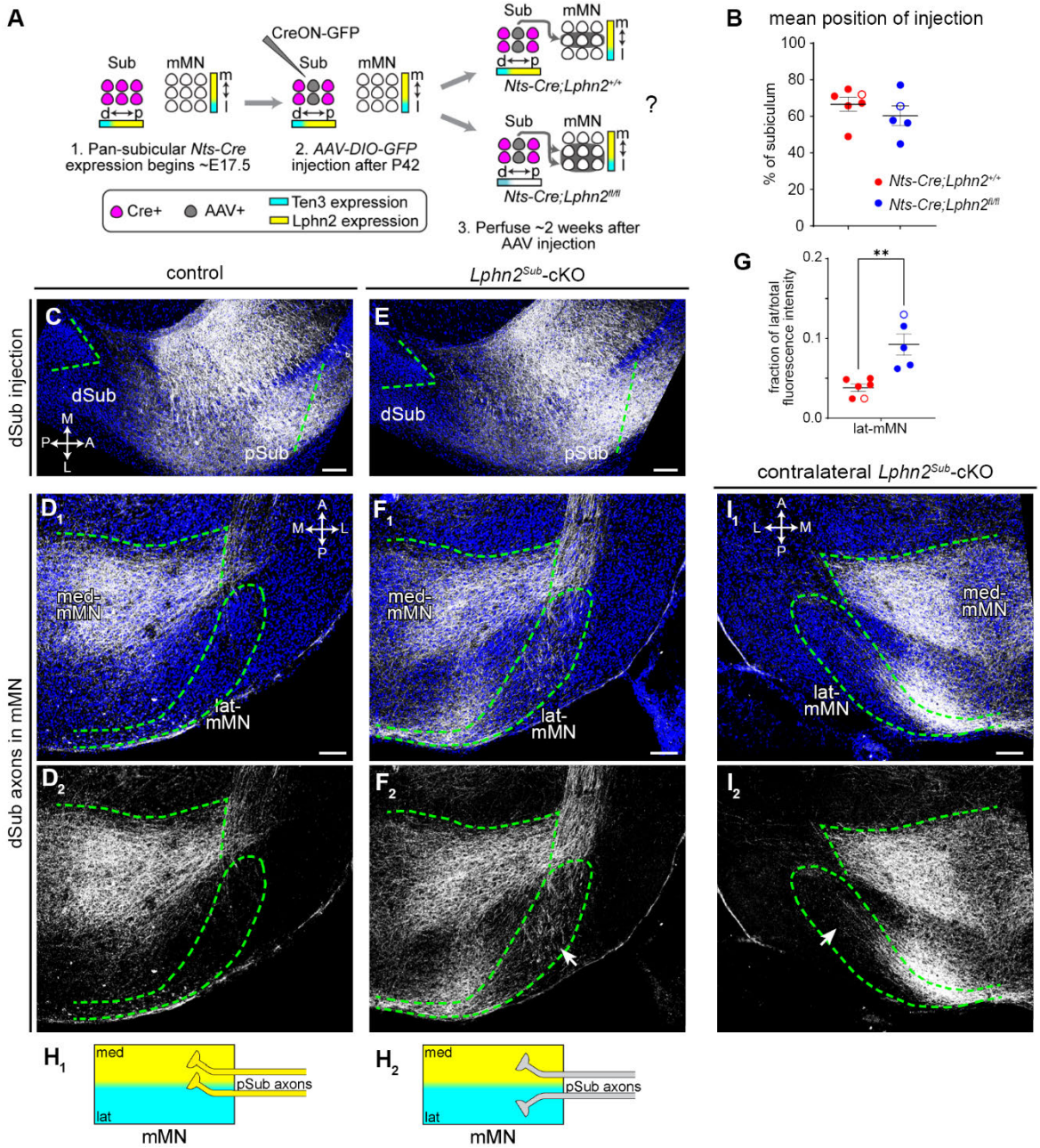

Figure 6. Lphn2 is required in subiculum for pSub axons to precisely target to medial mMN.
(A) Injection strategy and possible results for tracing proximal subiculum (pSub) axons into mMN of control (top right) and *Lphn2*^{Sub}-cKO mice (bottom right).
(B) Mean positions of injection sites along the distal-to-proximal axis of subiculum show no differences between controls (n = 6 mice) and *Lphn2*^{Sub}-cKO mice (n = 5 mice). Open circles indicate representative animals shown in C, E. Mean ± SEM. Mann-Whitney test, no significant differences.
(C) Representative image of the *AAV-mCh* (gray) injection site of controls show that the virus is predominantly restricted to pSub. Injection corresponds to animal in D.
(D) Representative images of projection of pSub axons (gray) into mMN of controls (D_1). Bottom panel shows axons without DAPI counterstain (D_2).
(E, F) Same as C, D, but for *Lphn2*^{Sub}-cKO mice. *Lphn2* cKO axons spread outside of med-mMN and into lat-mMN (arrow in F_2).

(G) Fraction of total projection intensity of pSub axons in lat-mMN of controls (n=6; red) and *Lphn2*^{Sub}-cKO (n=5; blue). Open circles indicate representative animals shown in D, F. Mean ± SEM. Mann-Whitney test, ** $p < 0.01$.
(H) Schematic summary of target selection of pSub axons in mMN of control (H_1) and *Lphn2*^{Sub}-cKO (H_2) mice based on results in C–G.
(I) Same as F, but for projections into contralateral mMN. Contralateral *Lphn2* cKO axons spread into lat-mMN (arrow in I_2).
Scale bars, 100 µm. Anatomical borders were drawn based on DAPI counterstain (Figure S5H).
See Figure S3 for additional data. See Table S1 for detailed genotypes.

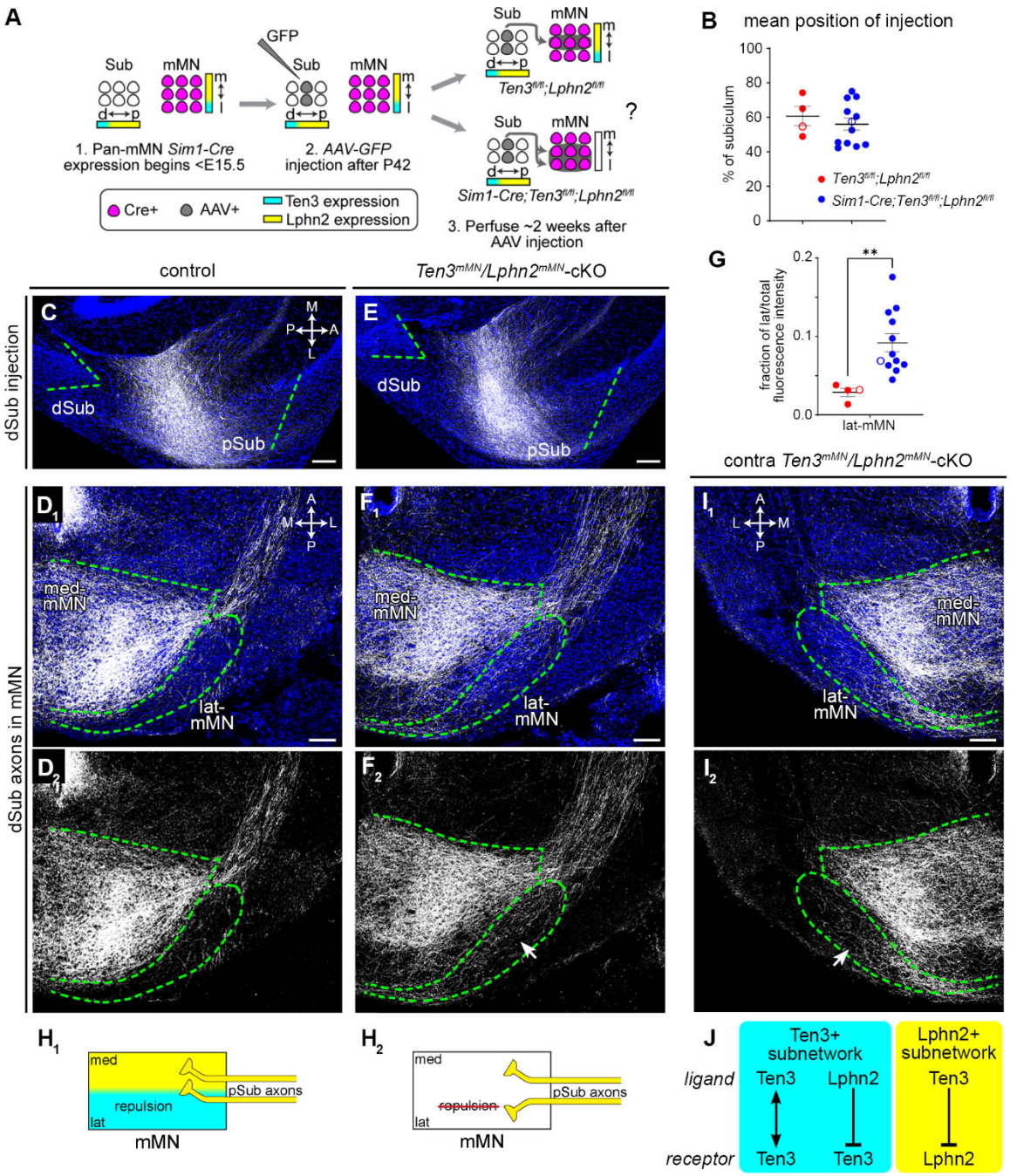

Figure 7. Ten3/Lphn2 are required in mMN for the precise targeting of pSub axons.

(A) Injection strategy and possible results for tracing pSub axons into mMN of control (top right) and *Ten3*^{mMN}/*Lphn2*^{mMN}-cKO mice (bottom right).

(B) Mean positions of injection sites along the distal-to-proximal axis of subiculum show no differences between controls (n=4, red) and *Ten3*^{mMN}/*Lphn2*^{mMN}-cKO (n=12, blue). Open circles indicate representative animals shown in C, E. Mean ± SEM. Mann-Whitney test, no significant differences.

(C) Representative image of the *AAV-mCh* (gray) injection site of controls show that the virus is predominantly restricted to pSub. Injection corresponds to animal in (D).

(D) Representative images of projection of pSub axons (gray) into mMN of control mice (D_1). Bottom panel shows axons without DAPI counterstain (D_2).

(E, F) Same as C, D, but for *Ten3*^{mMN}/*Lphn2*^{mMN}-cKO mice. Lphn2^{+} pSub axons spread into lat-mMN (arrow in F_2).

(G) Fraction of total projection intensity of pSub axons in lat-mMN of controls (n = 4 mice, red) and *Ten3*^{mMN}/*Lphn2*^{mMN}-cKO (n = 12 mice, blue). Open circles indicate representative animals shown in D, F. Mean ± SEM. Mann-Whitney test, ** $p < 0.01$.
(H) Schematic summary of target selection of pSub axons in mMN of control (H_1) and *Ten3*^{mMN}/*Lphn2*^{mMN}-cKO (H_2) mice based on results in C–G.
(I) Same as F, but for projections into contralateral mMN. Lphn2$^+$ pSub axons spread into contralateral lat-mMN of *Ten3*^{mMN}/*Lphn2*^{mMN}-cKO mMN (arrow in I_2).
(J) Summary of the Ten3–Lphn2 molecular module. Originally established in a CA1→Sub projection, this study demonstrates its broad use across the extended hippocampal network.
Scale bars, 100 μm. Anatomical borders were drawn based on DAPI counterstain (Figure S5H).
See Figures S3 for additional data. See Table S1 for detailed genotypes.

STAR METHODS

Key Resource Table

REAGENT or RESOURCE	SOURCE	IDENTIFIER
Antibodies		
Rabbit monoclonal anti-HA-tag (C29F4)	Cell Signaling Technology	Cat#3724; RRID:AB_1549585
Sheep polyclonal anti-GFP	Bio-Rad Laboratories	Cat#4745-1051; RRID:AB_619712
Chicken polyclonal anti-GFP	Aves Labs, Inc	Cat#GFP-1020; RRID:AB_10000240
Rat monoclonal anti-mCherry (16D7)	ThermoFisher Scientific	Cat#M11217; RRID:AB_2536611
Rabbit polyclonal anti-RFP	Rockland	Cat#600-401-379; RRID:AB_2209751
Guinea pig polyclonal anti-Cre-recombinase	Synaptic Systems	Cat#257 005; RRID:AB_2943537
Bacterial and virus strains		
LV-CAG-Cre-GFP	SignaGen Laboratories	Cat#SL100283
AAV8-EF1a-DIO-hChR2(H134R)-eYFP	Stanford University Gene Vector and Virus core; Fenno et al.[55]	custom
AAV-EF1a-FAS-hChR2(H134R)-mCherry	Gene Vector and Virus core, Stanford University; Saunders et al.[56]	custom
AAV8-EF1a-DIO-hChR2(H134R)-mCherry-WPRE-HGHpA	Addgene	Cat#20297-AAV8
AAV8-hSyn-hChR2(H134R)-mCherry	Addgene	Cat#26976-AAV8
AAV8-Syn-ChR2(H134R)-GFP	AddGene; Boyden et al.[57]	Cat#58880-AAV8
Chemicals, peptides, and recombinant proteins		
5-(and-6)-tetramethylrhodamine biocytin	ThermoFisher Scientific	Cat#T12921
Critical commercial assays		
RNAscope Multiplex Fluorescent Reagent Kit v2	ACD Bio; Wang et al.[39]	Cat#323100
RNAScope Probe: *Tenm3*	ACD Bio	Cat#411951
RNAScope Probe: *Lphn2*	ACD Bio	Cat#319341
Deposited data		
Raw and analyzed data	This paper	Available upon request
Experimental models: Organisms/strains		
Mouse: Ten3$^{HA/HA}$	Companion paper; Chon, Pederick et al.[37]	NA
Mouse: Lphn2$^{mVenus/mVenus}$	Anderson et al.[38]	NA
Mouse: Nts-Cre: B6;129-*Nts*$^{tm1(cre)Mgmj}$/J	The Jackson Laboratory; Leinninger et al.[58]	RRID:IMSR_JAX:017525

Mouse: Sim1-Cre: Tg(Sim1-cre)1Lowl/J	The Jackson Laboratory; Balthasar et al.[59]	RRID:IMSR_JAX:006395
Mouse: Ten3$^{fl/fl}$: *Tenm3*$^{em2.1Luo}$/J	The Jackson Laboratory; Berns et al.[8]	RRID:IMSR_JAX:031705
Mouse: Lphn2$^{fl/fl}$: B6;129S6-*Adgrl2*^{tm1Sud}/J	The Jackson Laboratory; Anderson et al.[38]	RRID:IMSR_JAX:023401
Mouse: Ai75D: B6.Cg-*Gt(ROSA)26Sor*$^{tm75.1(CAG-tdTomato*)Hze}$/J	The Jackson Laboratory; Quina et al.[60]	RRID:IMSR_JAX:025106
Mouse: CD1 wildtype	Charles River Laboratories	
Software and algorithms		
Fiji (ImageJ)	NIH	https://imagej.net/software/fiji/
MATLAB R2023b	MathWorks	https://www.mathworks.com/products/matlab.html
Custom normalization code (MATLAB)	Pederick et al.[9]	https://github.com/dpederick/Reciprocal-repulsions-instruct-the-precise-assembly-of-parallel-hippocampal-networks
Prism 10	GraphPad	https://www.graphpad.com/

RESOURCE AVAILABILITY

Lead contact

Further information and requests for resources should be directed to the lead contact, Liqun Luo (lluo@stanford.edu)

Materials availability

This study did not generate new unique reagents.

Data and code availability

Data reported in this paper are available from lead contact upon request. Data was normalized using custom MATLAB code (resample.m), previously published in Pederick et al. 2021[9] and can be found here: https://github.com/dpederick/Reciprocal-repulsions-instruct-the-precise-assembly-of-parallel-hippocampal-networks

EXPERIMENTAL MODEL AND STUDY PARTICIPANTS

Protein expression and *ex vivo* injection experiments used *Ten3*$^{HA/HA}$;*Lphn2*$^{mVenus/mVenus}$ mice at postnatal day 0 (P0) and P8.[37,38] CD-1 mice from Charles River Laboratories were used for double *in situ* hybridization and *ex vivo* tracing timeline experiments, ages ranging from embryonic day 15.5 (E15.5) to P6. All loss-of-function (LOF) experiments used crosses of *Nts-Cre* (C57BL/6 and 129/SvJ mixed background; JAX #017525),[58] *Sim1-Cre* (C57BL/6, 129/SvJ, and FVB mixed background; JAX #006395),[59] *Ten3*$^{fl/fl}$ (mixed background C57BL/6, 129/SvJ, and CD1),[8] *Lphn2*$^{fl/fl}$ (mixed background C57BL/6, 129/SvJ, and CD1).[38] Cre lines were characterized

at E15.5, E17.5, P0 and adult using Ai75D nuclear reporter mice (*Rosa-CAG-LSL-ntdTomato::deltaNeo*; C57BL/6; JAX stock #025106).[60] Genotypes used for each experiment are listed in detail in Table S1.

For the entorhinal cortex→subiculum and entorhinal cortex→CA1 *Ten3* deletion in axons (CreON/CreOFF) experiments (Figure 2, Figure S2), breeder pairs were maintained to produce all homozygous litters due to the low probability of correctly injecting overlapped P0 lentivirus and adult AAVs. Thus, these animals were not randomly allocated to experimental groups and were instead compared to age-matched CD1 wildtypes. Randomly allocated littermate controls were used for all other loss-of-function experiments conducted at P42 or later.

Due to low efficiency and strict cut off criteria, the total number of mice injected and screened for each experiment is as follows: Figure 2/Figure S2: 161 *Ten3*$^{+/+}$ and 181 *Ten3*$^{fl/fl}$; Figure 3/Figure S4: 73 *Nts-Cre;Ten3*$^{fl/fl}$*;Lphn2*$^{fl/fl}$ and controls, 136 *Nts-Cre;Lphn2*$^{fl/fl}$ and controls, and 43 *Nts-Cre;Ten3*$^{fl/fl}$ and controls; Figure 4/Figure S5: 132 *Nts-Cre;Ten3*$^{fl/fl}$ and controls; Figure 5/Figure S6: 62 *Sim1-Cre;Ten3*$^{fl/fl}$*;Lphn2*$^{fl/fl}$ and controls, 67 *Sim1-Cre;Lphn2*$^{fl/fl}$ and controls, and 55 *Sim1-Cre;Ten3*$^{fl/fl}$ and controls; Figure 6: 40 *Nts-Cre;Lphn2*$^{fl/fl}$ and controls.

Male and female mice were used for all experiments. Mice were group-housed on a 12 hr light/dark cycle with *ad libitum* access to food and water. All animal and virus procedures followed guidelines approved by Stanford University's Administrative Panel on Laboratory Animal Care and Administrative Panel on Biosafety in accordance with NIH guidelines.

METHOD DETAILS

Immunostaining

Animals were anesthetized with 2.5% Avertin (intraperitoneal) and transcardially perfused with 10 mM PBS, followed by 4% paraformaldehyde (PFA). Brains were dissected and post-fixed in 4% PFA for 1–2 hours (P0, P8) or 4–6 hours (>P42), then cryo-protected for at least 48 hours in a 30% sucrose solution. E15.5 and E17.5 brains for Cre characterizations (Figure S3) were fresh-dissected and post-fixed in 4% PFA overnight before cryoprotection. Brains were embedded in Optimum Cutting Temperature (OCT)-filled cryomolds in a 2-methylbutane bath, cooled by dry ice and stored at –80°C until sectioning. Serial 60-µm horizontal sections were collected free-floating in 24-well plates in a solution of 10 mM PBS and 0.02% sodium azide and stored at 4°C until staining. CD1 wildtype *ex vivo* injections were sectioned at 180-µm (see '*Ex vivo* injections' for more details). The staining procedure was as follows: Incubation in (1) 10 mM PBS for 3× 10 min washes at room temperature (RT), (2) blocking solution of 0.3% PBST and 10% normal donkey serum (NDS) for 1–2 hours RT, (3) primary antibody in 0.3% PBST for 2–3 nights at 4°C, (4) 0.3% PBST for 3× 10 min washes RT, (5) secondary antibody in 0.3% PBST and 10% NDS block for 1–2 hours RT, (6) DAPI (1:5000 dilution of 5 mg/mL; Invitrogen) in 0.3% PBST for 15 min RT, and (7) 10 mM PBS for 3× 10 min washes RT. Sections were mounted in 10 mM PBS and cover-slipped using ProLong Gold Antifade Mountant (Invitrogen). Primary antibodies include: Rabbit anti-HA (1:300, Cell Signaling #3724), Sheep GFP (1:1500, BioRad 4745-1051), chicken anti-GFP (1:1000, Aves Labs, GFP-1020), rat anti-mCherry (1:1000, ThermoFisher, M11217), rabbit anti-RFP (1:1000, Rockland 600-401-379), and guinea pig anti-Cre-recombinase (1:500, Synaptic Systems 257 005). Secondary antibodies used were species-specific conjugated antibodies: AlexaFluor 488 (1:1000, Invitrogen), Cy3 Affinipure (1:1000, Jackson ImmunoResearch), AlexaFluor 647 (1:1000, Invitrogen). Images were taken with a Zeiss LSM 900 confocal microscope. For quantification details see 'Image and data analysis' sections.

Double *in situ* hybridization (RNAScope)

E15.5, E17.5, and P0 pups were sacrificed by rapid decapitation. For embryonic dissections, pregnant dams were anesthetized with isoflurane before cervical dislocation and uterine dissection. Brains were fresh-dissected in ice-cold 10 mM PBS and immediately embedded and frozen in OCT-filled cryomolds in a 2-methylbutane bath, cooled by dry ice. Brains were stored at –80°C until sectioning. Serial 12-µm horizontal sections were collected on Superfrost Plus slides (Fisher Scientific) and stored at –20°C until procedure. Double *in situs* were performed

using the RNAscope Multiplex Fluorescent Reagent Kit v2 (ACD Bio)[39] and performed according to RNAScope assay guidelines for fresh-frozen samples with the following modifications for neonatal tissue during pretreatment: Sections were fixed on slides for 90 minutes in 4% PFA and Protease III was used during the digestion step. Probes used were RNAScope Probe- Mm-Tenm3 (1:2, ACD Bio 411951) and RNAScope Probe-Mm-Lphn2-C2 (1:100, ACD Bio 319341-C2). Fluorophores used were Opal Dye 570 (1:1500, Akoya Biosciences) and Opal Dye 690 (1:1500, Akoya Biosciences). Images were taken with a Zeiss LSM 900 confocal microscope (10× objective, with 0.5× digital zoom).

***Ex vivo* injections**

For embryonic dissections, pregnant dams were anesthetized with isoflurane before cervical dislocation and uterine dissection. Pups were sacrificed by rapid decapitation individually at the time of injection. Brains were fresh-dissected into ice-cold artificial cerebrospinal fluid (ACSF) that contained (in mM) 110 choline chloride, 2.5 KCl, 1.2 NaH_2PO_4, 20 HEPES, 5 sodium ascorbate, 2 thiourea, 3 sodium pyruvate, 1 $CaCl_2$, 1.3 $MgCl_2$, 26.8 $NaHCO_3$, 25 glucose, and 73 trehalose. A scalpel was used to crudely remove olfactory bulbs and the most rostral ~1/4 of the brain to create a flat surface as well as any midbrain and hindbrain structures obscuring the caudal surface of cerebral cortex. Brains were pinned with caudal surface exposed in a silicon-lined dissecting dish filled with ice-cold ACSF. Using exterior anatomy as a guide, 5% 5-(and-6)-tetramethylrhodamine biocytin in 0.9% saline (biocytin TMR; Invitrogen) was iontophoretically injected into the approximate location of medial entorhinal cortex. Iontophoresis was performed for 3 min at 5 µA current using glass pipette tips with an outside diameter of 15–20-µm. Brains were then placed in carbogenated ACSF at RT for ~6 hours, covered to protect from light, to allow time for dye to spread to axon terminals. After 6 hours, brains were placed in 4% PFA overnight to fix and moved to 30% sucrose solution for 24–48 hours for cryoprotection. Brains were embedded, sectioned, and stained as described previously (see 'Immunostaining'), but were sectioned at 180-µm for axon tracing in wildtype animals to visualize more of the axon trajectory in one plane (Figure S1C, D).

Stereotactic injections in neonatal pups

Pups were anesthetized via hypothermia and mounted in stereotactic apparatus modified to hold them. Cranial anatomy was visualized through the skin for stereotactic coordinates and a small incision was created using a 27-gauge needle in place of a craniotomy. Stereotactic coordinates were measured from lambda. MEC coordinates were 2.05–2.15 mm lateral, 0.6–0.65 mm posterior, and 1.4–1.45 mm ventral from brain surface. 400 nL of *LV-CAG-Cre-GFP* (~6.6×10^8 copies/mL; SignaGen SL100283) was injected at 100 nl/min.

Stereotactic injections in adult mice

P42 or older mice were anesthetized using isoflurane and mounted in stereotactic apparatus. Virus was injected via iontophoresis (5 uA current, 7 s on/7 s off) for 2 min using glass pipette tips with an outside diameter of 10–15-µm. Mice were perfused 2–3 weeks post-injection and processed as described above (see 'Immunostaining'). Stereotactic coordinates were all measured from lambda and vary based on strain, genotype, and age. MEC coordinates were 2.75–3.1 mm lateral, 0.475–0.675 mm posterior, and 2.05–2.2 mm ventral from brain surface. Distal subiculum (dSub) coordinates were 2.8–2.9 mm lateral, 0.175 mm posterior to 0.05 mm anterior, and 1.95–2.05 mm ventral from brain surface. Medial subiculum (mSub) coordinates were 3.05–3.1 mm lateral, 0.2–0.525 mm anterior, and 1.95–2.05 mm ventral from brain surface. Viruses injected were as follows: *AAV8-EF1a-DIO-hChR2(H134R)-eYFP* (*CreON-GFP*; 2 $\times 10^{12}$–1×10^{13} copies/mL; Gene Vector and Virus core, Stanford University)[55], *AAV8-EF1a-FAS-hChR2(H134R)-mCherry* (*CreOFF-mCh*; 2–8×10^{12}; Gene Vector and Virus core, Stanford University),[56] *AAV8-EF1a-DIO-hChR2(H134R)-mCherry-WPRE-HGHpA* (*CreON-mCh*; 4×10^{12}–1.2×10^{13} copies/mL; gift from Karl Deisseroth, Addgene viral prep # 20297-AAV8), *AAV8-hSyn-hChR2(H134R)-mCherry* (*AAV-mCh*; 1×10^{13} copies/mL gift from Karl Deisseroth, Addgene viral prep # 26976 -AAV8), and *AAV8-Syn-ChR2(H134R)-GFP* (*AAV-GFP*; 1×10^{13} copies/mL; gift from Edward Boyden, Addgene viral prep # 58880-AAV8).[57]

QUANTIFICATION AND STATISTICAL ANALYSIS

Image and data analysis for entorhinal cortex→subiculum axon tracing

Images of injection sites (10× magnification) and projections (10× objective, with 0.45× digital zoom) were acquired for every other 60-µm section using a Zeiss LSM 900 confocal. Images of direction of axons entering subiculum at P0 were taken at 20× with 0.5× digital zoom (Figure S1E). Due to variations in injection sites and time lapse between experiments, exposures were adjusted for each mouse and fluorescence intensity was normalized post hoc for comparison. Fluorescence intensity and injection position measurements were performed on unprocessed images and collected using FIJI. Data processing was performed in MATLAB and Excel.

Strict inclusion criteria were applied to ensure tracing only from the appropriate subnetwork (Ten3$^+$ MEC). Inclusion criteria were as follows: (1) Both AAV injection sites must be in medial entorhinal cortex (mean position within most medial 20% of entorhinal cortex)—based on Ten3 mRNA in horizontal entorhinal section[9]; (2) lentivirus *Cre-GFP* injection must allow for roughly equal expression of *AAV-CreON-GFP* and *AAV-CreOFF-mCh;* (3) 3 brightest sections of *AAV-CreON-GFP* and *AAV-CreOFF-mCh* must overlap by 2 of 3 sections across the dorsal–ventral axis; (4) lentivirus Cre-GFP expression in subiculum and CA1 must be minimal. Animals that fulfilled these criteria were included in the quantifications reported in Figures 2, 3 and Figures S2, 4.

For injection site quantification, all image and data processing were done using FIJI. First, a 425-pixel-wide segmented line was drawn from medial to lateral of layer II/III entorhinal cortex using DAPI counterstain to define edges. The segmented lines from each channel in the image were straightened using the Straighten function. Background subtraction was done by measuring the mode value of background regions and using the Subtract function to remove the mode value. The Plot Profile command was then used to extract fluorescence intensity (FI) along the medial–lateral axis. To compare across animals, these FI plots were resampled into 100 equal bins representing the length of entorhinal cortex using a custom MATLAB code.[8,9] The FI traces of the three brightest sections of injection site were summed together and normalized to FI values of 0–100. The mean position of the injection site was calculated by multiplying the FI value by its bin position, summing across the entire axis, and dividing by the sub of FI values.

Because *LV-Cre-GFP* may extend past the *AAV-CreON-GFP* tracing injection, it contributes fluorescence that would influence the calculation for AAV injection mean position. To resolve this, all animals were stained with a Cre antibody in the far-red channel that was also processed as above. The image calculator function was used to subtract the Cre only channel from the GFP channel to remove any GFP being contributed by Cre-GFP before the Plot Profile was extracted.

Projection site processing and quantification was done similarly to the injection site quantification, but the initial line was drawn as a 50-pixel wide segmented line along the distal–proximal axis of subiculum molecular layer and a 100-pixel-wide segmented line along the distal–proximal axis of CA1 molecular layer. Although it is impossible to avoid including axons occasionally traversing the space between subiculum and CA1, they are relatively uniform across genotype and account for only a small fraction of FI. Areas under the curve for subiculum FI traces were calculated in GraphPad Prism 10.

Image and data analysis for subiculum→mMN expression and topography

All images were acquired for every other 60-µm section using a Zeiss LSM 900 confocal (subiculum/mMN P8 Ten3–Lphn2 expression and adult subiculum injection site (10× objective, with 0.5× digital zoom); adult mMN projection site (10× objective, with 0.45× digital zoom). Hippocampal-entorhinal image shown (Figure 1B) is at 10× magnification. Images of axon tract and direction of axons entering mMN at P0 were taken at 20× with 0.5× digital zoom (Figure S1F, G).

For subiculum P8 Ten3–Lphn2 expression quantification, a 150-pixel-wide segmented line was drawn along the distal–proximal axis of the subiculum cell body layer using DAPI counterstain to define edges. The segmented line was straightened, background subtracted, quantified, and the data processed as described for MEC injection above (see 'Image and data analysis for subiculum→mMN axon tracing'). Six sections from one animal

(Figure 1B$_1$) are represented as Ten3 and Lphn2 fluorescence intensity traces (Figure S1A$_1$). For mMN P8 Ten3–Lphn2 expression quantification, a 250-pixel-wide segmented line was drawn along the Ten3–Lphn2 gradient (posterolateral to anteromedial) and processed in the same way. Three sections from one animal (Figure 1B$_2$) are represented as Ten3 and Lphn2 fluorescence intensity (Figure S1A$_2$).

In FIJI, a 125-pixel-wide segmented line was drawn for adult subiculum injection site, and a 250-pixel-wide segmented line was drawn for adult mMN projection site quantification. Both were processed as above, but a heatmap was generated in Prism 10 for opposing mCherry (dSub) and GFP (pSub) injection (Figure S1A$_1$) and projection site intensity (Figure S1A$_2$). Three sections from one animal (Figure 1C) are represented for each.

Image and data analysis for subiculum→mMN axon tracing

Images of injection sites (10× objective, with 0.5× digital zoom) and projections (10× objective, with 0.45×x digital zoom) were acquired for every other 60-µm section using a Zeiss LSM 900 confocal. Due to variations in injection sites and time lapse between experiments, exposures were adjusted for each mouse and fluorescence intensity was normalized post hoc for comparison. Fluorescence intensity and injection position measurements were done on unprocessed images and collected using FIJI. Data processing was performed in MATLAB and Excel.

Strict inclusion criteria were applied to ensure tracing only from the appropriate subnetwork. Inclusion criteria for Ten3$^+$ dSub tracing is that AAV injection site must be in the most distal 20% of subiculum by mean position for sparse axon tracing (Figure S5) or between 12% and 20% for region-based analyses (Figures 4, 5). Animals that fulfilled these criteria were included in the quantifications reported in Figures 4, 5 and Figures S5, 6. Inclusion criteria for Lphn2$^+$ pSub are as follows: AAV injection site (1) must be between 40–80% of subiculum by mean position and (2) must have less than 10% of its total fluorescence within dSub (distal 20% of subiculum). Animals that fulfilled these criteria were included in the quantifications reported in Figures 6 and 7. These criteria are based on Ten3 and Lphn2 mRNA in horizontal subiculum sections.[9]

For injection site quantification, a 125-pixel-wide segmented line was drawn along the distal–proximal axis of the subiculum cell body layer using DAPI counterstain to define edges. The segmented line was straightened, background subtracted, quantified, and the data processed as described for MEC above (see 'Image and data analysis for subiculum→mMN axon tracing'), except for Cre-related fluorescence subtraction.

For projection site quantification, regions of interests (ROIs) of lat-mMN and med-mMN were drawn using the DAPI counterstain to define edges **(Figure S5H).** Background subtraction was done by measuring mean fluorescence intensity of background and using the Subtract function to delete it. Images were binarized and then the total fluorescence intensity of each ROI was collected using the raw integrated density measurement. Data is represented as the ratio of fluorescence intensity in lat-mMN or med-mMN over total fluorescence intensity in mMN.

Rank order data analysis for dSub→lat-mMN axon tracing

Imaging, inclusion criteria, and image and data processing for subiculum injection site is the same as above. Imaging and image processing for mMN projection is same as above (see 'Image and data analysis for subiculum→mMN axon tracing'). For rank order analysis, the total fluorescence intensity was collected from unprocessed images using the raw integrated density measurement in FIJI for each mMN. The two brightest ipsilateral and two brightest contralateral sections of mMN for each animal were auto-balanced using the brightness/contrast adjustment tool in FIJI to enhance the contrast of single axons. An independent researcher, blinded to genotype, numbered all ipsilateral and all contralateral images from most severe mistargeting (#1) to no mistargeting (#16), accounting for the amount of axons within the axon tract as a proxy for injection site density. Animals were re-identified and rank-sum statistics were performed (Figure S5).

Statistics

Statistical tests were performed using GraphPad Prism 10. For sample sizes and details of statistical analyses, see figure legends. All experiments were randomized, except for the experiment of the entorhinal cortex→subiculum, *Ten3* deletion in axons (see 'Mice' for more details).

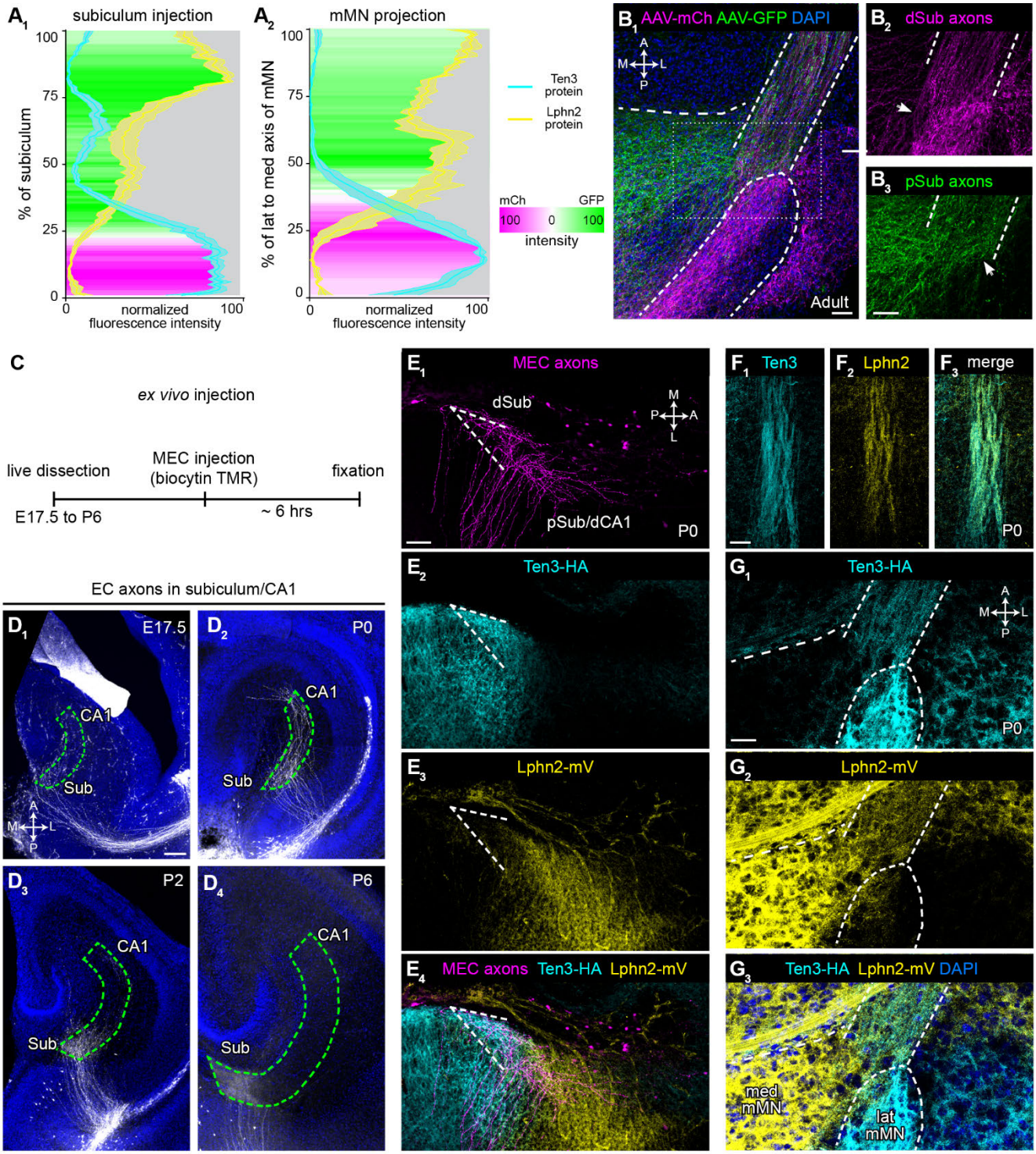

Figure S1. Additional data on axon tracing in adult and during development, related to Figure 1
(A) Quantitative depiction of dual-color anterograde tracing and Ten3/Lphn2 expression of subiculum→mMN projection in Figure 1B, C. (A_1) Normalized fluorescence intensity traces of Ten3 (cyan) and Lphn2 (yellow) protein expression along the distal-to-proximal axis of subiculum in P8 *Ten3*$^{HA/HA}$;*Lphn2*$^{mVenus/mVenus}$ mouse (Figure $1B_1$) overlaid with dSub (mCherry, magenta) and pSub (GFP, green) injection site density heatmap (Figure $1C_1$) and (A_2) a diagonal lat-mMN-to-med-mMN axis of mMN expression (Figure $1B_2$) overlaid with density heatmap of projections from dSub (magenta) and pSub (GFP; Figure $1C_2$). The correspondence between

axon intensity at the injection and projection sites and Ten3/Lphn2 expression supports the 'Ten3→Ten3, Lphn2→Lphn2' connectivity rule.

(B) Additional representative image of topographic projections in lat-mMN and med-mMN (B_1; from dual dSub and pSub injections), show axons do not segregate until reaching the target and then turn (arrows) to fill $Ten3^+$ (B_2) and $Lphn2^+$ subfields (B_3). B_2 and B_3 are from dotted rectangle in B_1, labeled only with mCherry or GFP channels, respectively. Scale bar, 50 µm.

(C) Schematic for *ex vivo* injections for developmental tracing of entorhinal cortex→subiculum projection.

(D) Representative images of projection of entorhinal cortex axons into the molecular layer of subiculum in wildtype animals at E17.5 (D_1), P0 (D_2), P2 (D_3), and P6 (D_4). Axons begin to invade subiculum at E17.5 and progressively increase in density through P6. Scale bar, 100 µm.

(E) Representative images of MEC axons (magenta) at P0 entering Ten3-high dSub (cyan) and turning before proceeding to Lphn2-high pSub (yellow) at P0. The three images are from the same confocal section showing axons (E_1), Ten3 protein (E_2), Lphn2 protein (E_3), and merge (E_4) channels. Scale bar, 50 µm.

(F) Representative images of subiculum axon tract at P0 along the path to mMN with extensive intermingling of $Ten3^+$ (cyan) and $Lphn2^+$ (yellow) axons in a $Ten3^{HA/HA}$; $Lphn2^{mVenus/mVenus}$ mouse. The three images are from the same confocal section showing Ten3 (F_1), Lphn2 (F_2), and merge (F_3) channels. Scale bar, 50 µm.

(G) Representative images of subiculum axon tract at P0, entering mMN target where axons experience $Ten3^+$ and $Lphn2^+$ subfields simultaneously. Ten3 (cyan) and Lphn2 (yellow) axons remain intermingled in the tract up until terminal projections in the target. The three images are from the same confocal section showing Ten3 (G_1), Lphn2 (G_2), and merge (G_3) channels. Scale bar, 25 µm.

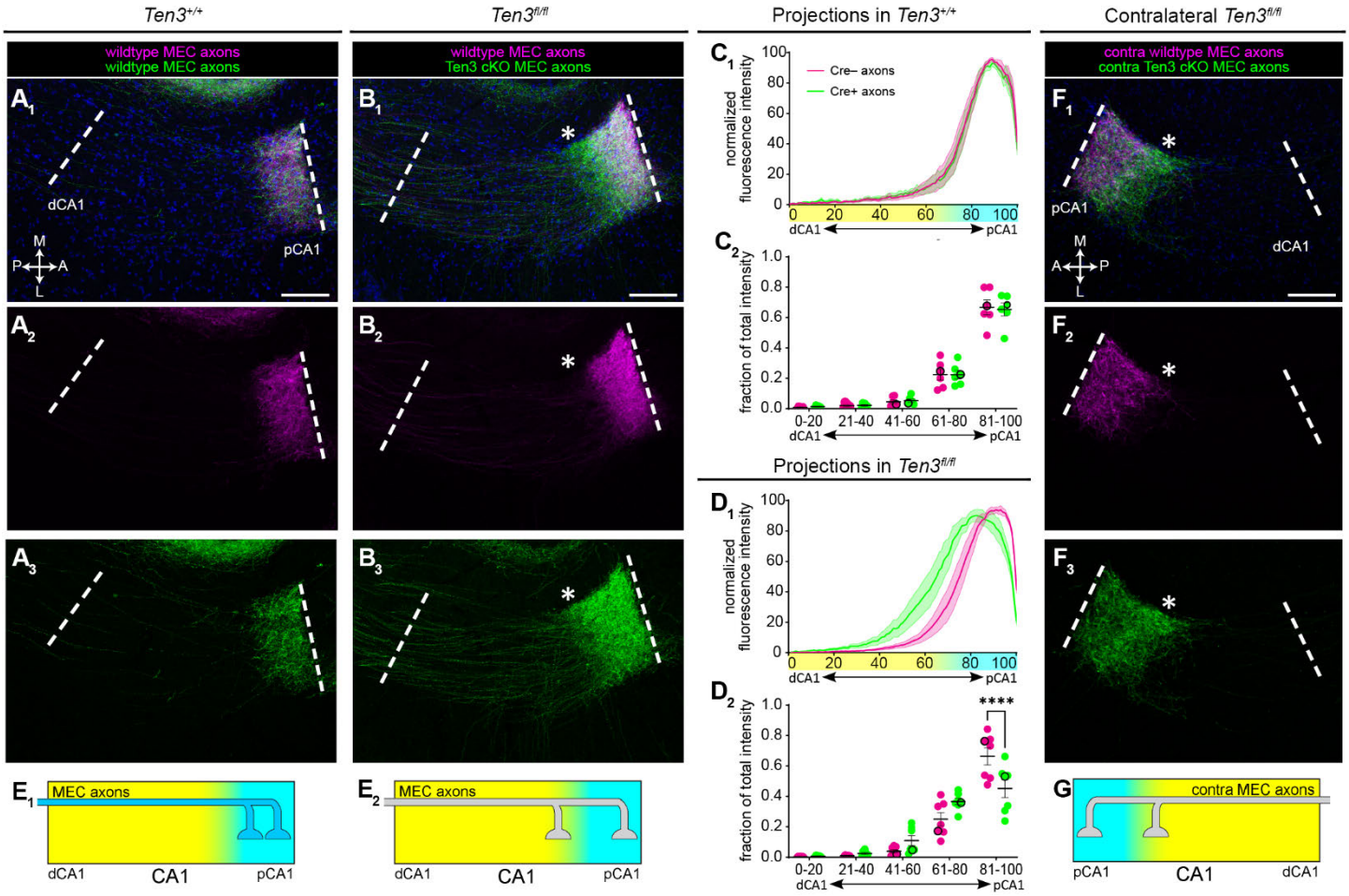

Figure S2. Additional analyses of the MEC axon projection, related to Figure 2

(A) Representative images of projection of Cre⁻ axons (magenta), and Cre⁺ axons (green) into molecular layer of CA1 in *Ten3*$^{+/+}$ controls. The three images are from the same confocal section showing merge (A_1), magenta only (A_2), or green only (A_3) channels. Corresponding injection site is shown in Figure 2C.

(B) Same as A but for *Ten3*$^{fl/fl}$ mice. *Ten3* cKO axons in *Ten3*$^{fl/fl}$ mice spread beyond the Cre⁻ control axons towards dCA1 (asterisk, in identical position across three images). Corresponding injection site is shown in Figure 2E.

(C_1) Normalized fluorescence intensity traces of the Cre⁻ (magenta) and Cre⁺ (green) projections along the distal→proximal axis of CA1 in *Ten3*$^{+/+}$ controls (n = 6 mice). Injection positions are shown in Figure 2B. Ten3 (cyan) and Lphn2 (yellow) expression is represented along the x-axis. Mean (dark line) ± SEM (shaded area).

(C_2) Fraction of total projection intensity (same as C_1) in 20% bins of CA1 axis of the Cre⁻ (magenta) and Cre⁺ (green) projections along the distal–proximal axis of CA1 in *Ten3*$^{+/+}$ controls (n = 6 mice). Injection positions are shown in Figure 2B. Black outlines indicate representative animal in A. Mean ± SEM. Two-way ANOVA corrected for multiple comparisons (Šídák correction), no significant differences.

(D) Same as C but for *Ten3*$^{fl/fl}$ (n = 7) mice. **** $p < 0.0001$.

(E) Schematic summary of target selection of MEC axons in CA1 in control (E_1) and *Ten3*^{MEC}-cKO (E_2) based on results in A–D.

(F) Same as B, but for projections into contralateral CA1. Contralateral Cre⁺, *Ten3*^{MEC}-cKO axons spread beyond the contralateral Cre⁻ control axons towards dCA1 (asterisk, in identical position across three images). Corresponding injection site is shown in Figure 2K.

(G) Schematic summary of target selection of MEC axons in contralateral CA1 in *Ten3*^{MEC}-cKO mice.

Scale bars, 100 μm.

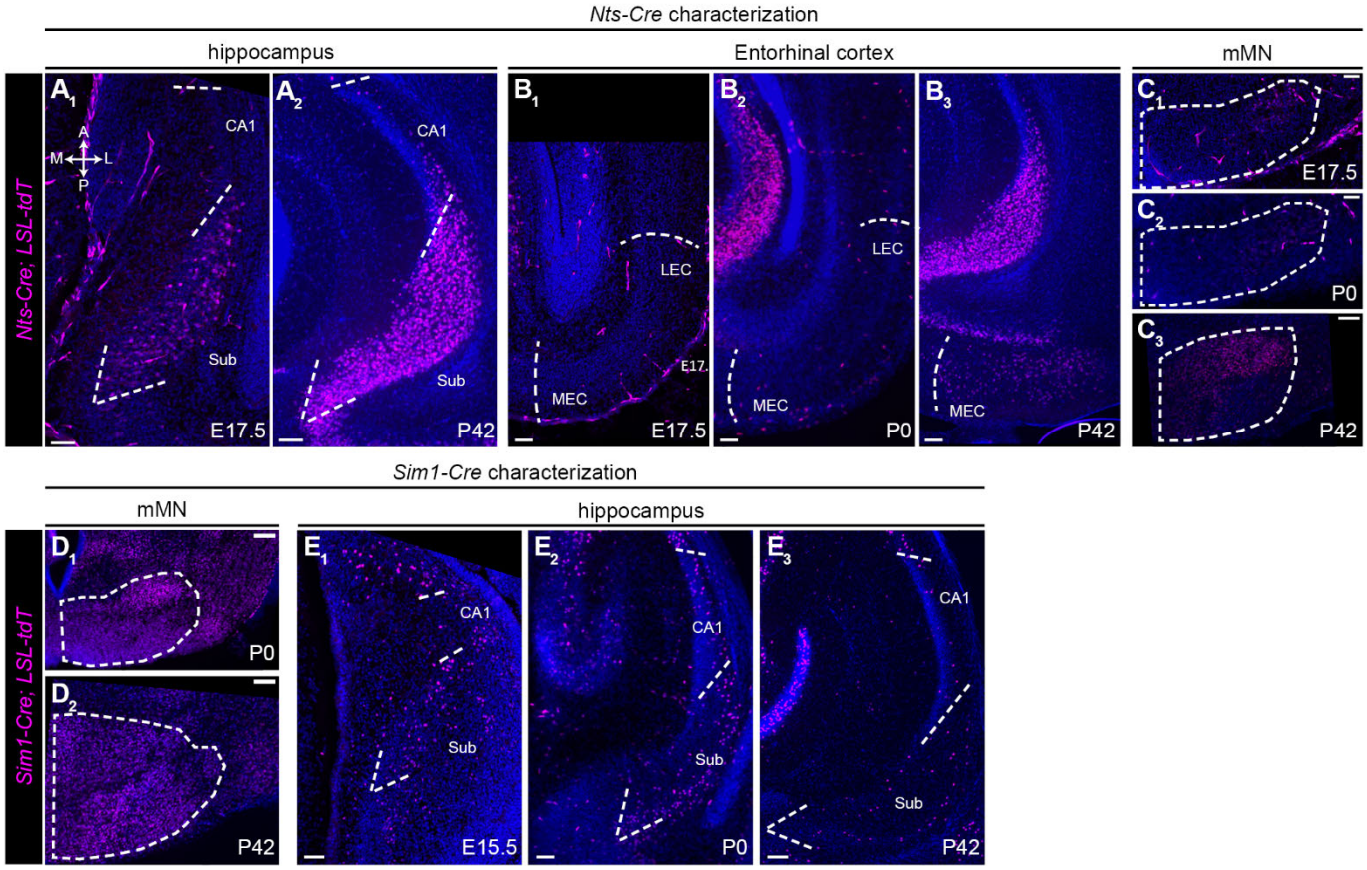

Figure S3. *Nts-Cre* and *Sim1-Cre* characterizations, related to Figures 3–7.

(A) Expression of *Nts-Cre* in subiculum and CA1, assessed by a nuclear tdTomato Cre reporter at E17.5 (A_1) and P42 (A_2). P0 data is in Figure 3A. The Cre reporter is sparsely expressed in subiculum at E17.5 and is denser by P0. Little CA1 expression is found even in adult. Scale bar, 50 µm (A_1), 100 µm (A_2).

(B) Same as A, except in entorhinal cortex with the addition of P0 (B_2). Expression is sparse in entorhinal cortex during development, ensuring target-only deletions in our examination of the MEC→dSub projection (Figure 3). Scale bar, 50 µm (B_1, B_2), 100 µm (B_3).

(C) Same as A, except in medial mammillary nucleus (mMN) with the addition of P0 (C_2). Expression is sparse in mMN during development, ensuring axon-only deletions in our examination of the subiculum→mMN projections (Figures 4 and 6). Scale bar, 50 µm (C_1, C_2), 100 µm (C_3).

(D) Expression of *Sim1-Cre* in mMN, assessed by a nuclear tdTomato Cre reporter at P0 (D_1) and P42 (D_2). E15.5 data is in Figure 5A. The Cre reporter is densely expressed in mMN by E15.5. Scale bars, 50 µm (D_1), 100 µm (D_2).

(E) Same as D, except in subiculum with the addition of E15.5 (E_1). Expression is sparse in subiculum during development and even in adults, ensuring target-only deletions in our examination of the subiculum→mMN projections (Figures 5 and 7). Scale bar, 50 µm (E_1, E_2), 100 µm (E_3).

All panels show endogenous tdTomato fluorescence, except for E17.5 *Nts-Cre* panels which are stained with RFP antibody (A_1, B_1, C_1).

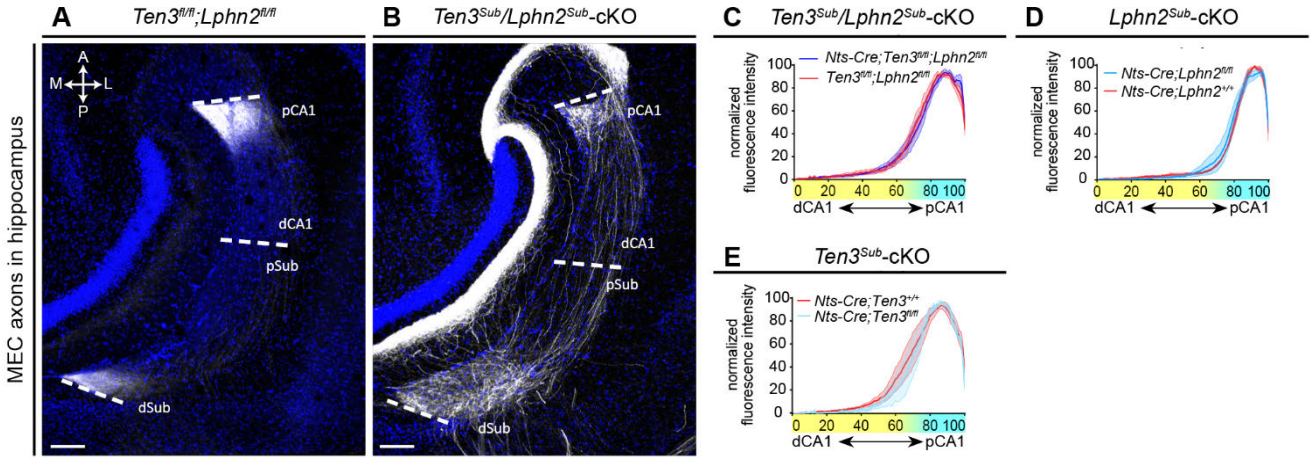

Figure S4. Normal targeting of MEC→pCA1 when in *Ten3/Lphn2* were conditionally knocked out in subiculum, related to Figure 3

(A) Representative image of MEC projections into molecular layer of CA1 and subiculum for controls. This is a larger field of view of Figure 3E to show that the same MEC axon population target both subiculum and CA1 with their terminals restricted to dSub and pCA1. Corresponding injection site is shown in Figure 2D. Scale bar, 100 μm.

(B) Same as A, but for *Ten3*^{Sub}*/Lphn2*^{Sub}-cKO mice. This is a larger field of view of Figure 3G$_1$. MEC axons spread towards pSub in subiculum but are restricted to pCA1 in CA1 as in control animals. Corresponding injection site is shown in Figure 2F.

(C) Normalized fluorescence intensity traces of MEC axon projections along the distal-to-proximal axis of CA1 internal controls (n = 7; red) and *Ten3*^{Sub}*/Lphn2*^{Sub}-cKO mice (n = 5; blue). Injection positions are shown in Figure 3C. Ten3 (cyan) and Lphn2 (yellow) expression is represented along the x-axis. Mean (dark line) ± SEM (shaded area).

(D) Same as C, but for control (n = 3; red) and *Lphn2*^{Sub}-cKO (n = 5; blue) mice.

(E) Same as C, but for control (n = 5; red) and *Ten3*^{Sub}-cKO (n = 4; blue) mice.

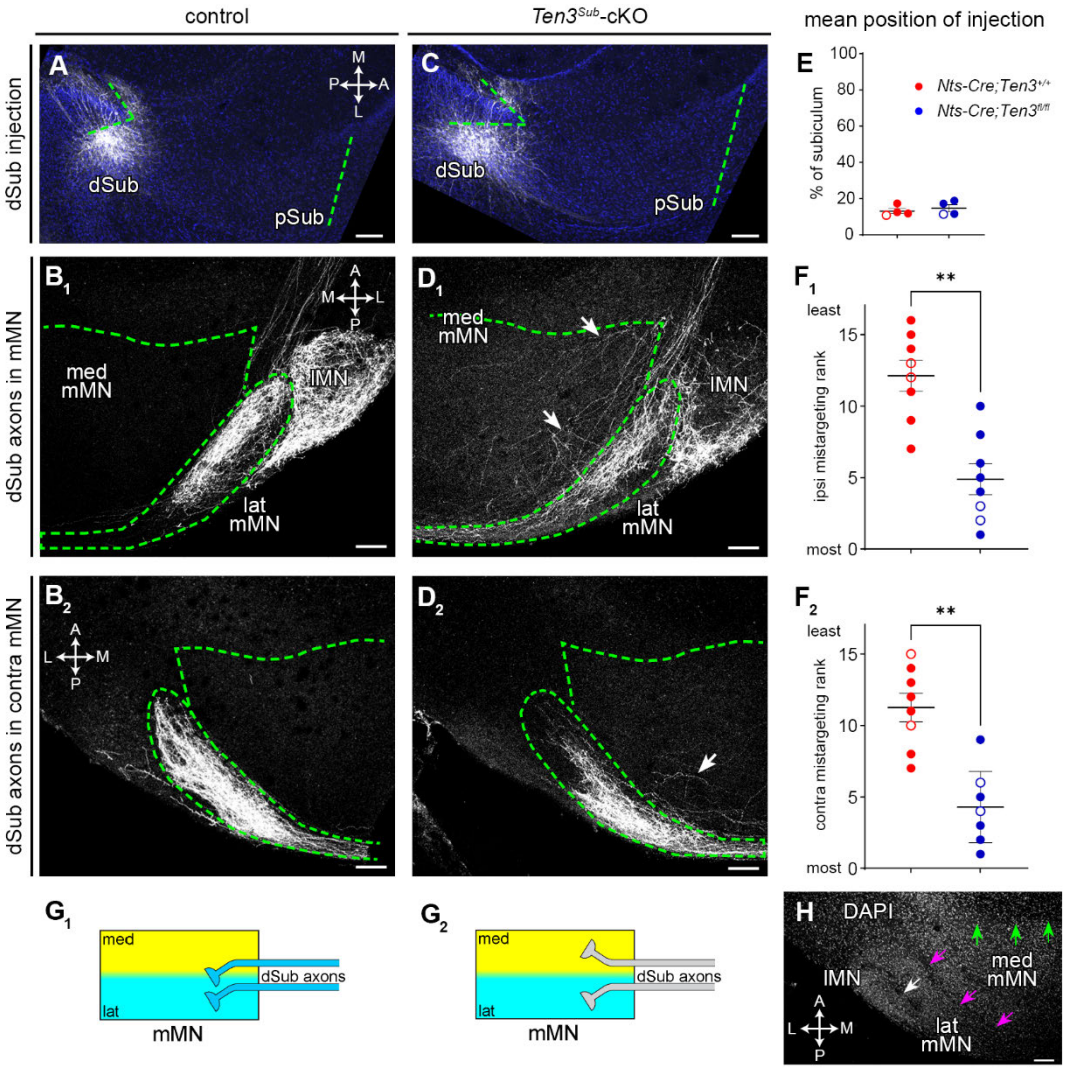

Figure S5. Additional *Ten3* axon deletion data to examine the dSub→lat-mMN projection, related to Figure 4.

In an independent set of experiments, we examined the phenotypes of dSub→lat-mMN projection in *Ten3*^{Sub}-cKO mice. Here, mistargeting of dSub axons into med-mMN in control and *Ten3*^{Sub}-cKO mice were rank-ordered by an experimenter blind to the genotype, based on the relative intensity of dSub axons in med-mMN and lat-mMN (to account for variations in injection intensity of anterograde tracers).

(A) Representative image of the *AAV-CreONmCh* (gray) injection site of controls show the virus is restricted to the most distal region of subiculum. Injection corresponds to animal in (B).

(B) Representative images of projection into ipsilateral (B_1) and contralateral (B_2) mMN of controls. Labeling in lateral mammillary nucleus (lMN) are unrelated axons from pre-subiculum.

(C, D) Same as A, B, but for *Ten3*^{Sub}-cKO mice. Even the most distal subiculum axons show aberrant branches in med-mMN (arrows in D).

(E) Mean positions of injection sites along the distal-to-proximal axis of subiculum show no differences between control (red) and *Ten3*^{Sub}-cKO (blue). Open circles indicate representative image in A, D. Mean ± SEM. Mann-Whitney test, no significant differences.

(F) Rank according to severity of mistargeting for control (red) and *Ten3*^{Sub}-cKO (blue) in ipsilateral (F_1) and contralateral (F_2) mMN. Open circles indicate representative animals in B, D. Ranked from most severe (1) to least severe (16). Mean ± SEM. Mann-Whitney test, ** $p < 0.01$.

(G) Schematic summary of target selection of dSub axons in contralateral mMN of control (G_1) and *Ten3*^{Sub}-cKO (G_2) mice based on results in A–F.

(H) Representative image of DAPI counterstain in mMN illustrates borders of sub-nuclei used to select regions of interest. Border of lMN (not studied) and lat-mMN (white arrow). Border of Ten3^{+} lat-mMN and Lphn2^{+} med-mMN (magenta arrows). Border of med-mMN and pre-mammillary nucleus (green arrows). Same section as Figure 4I.
Scale bars, 100 μm.

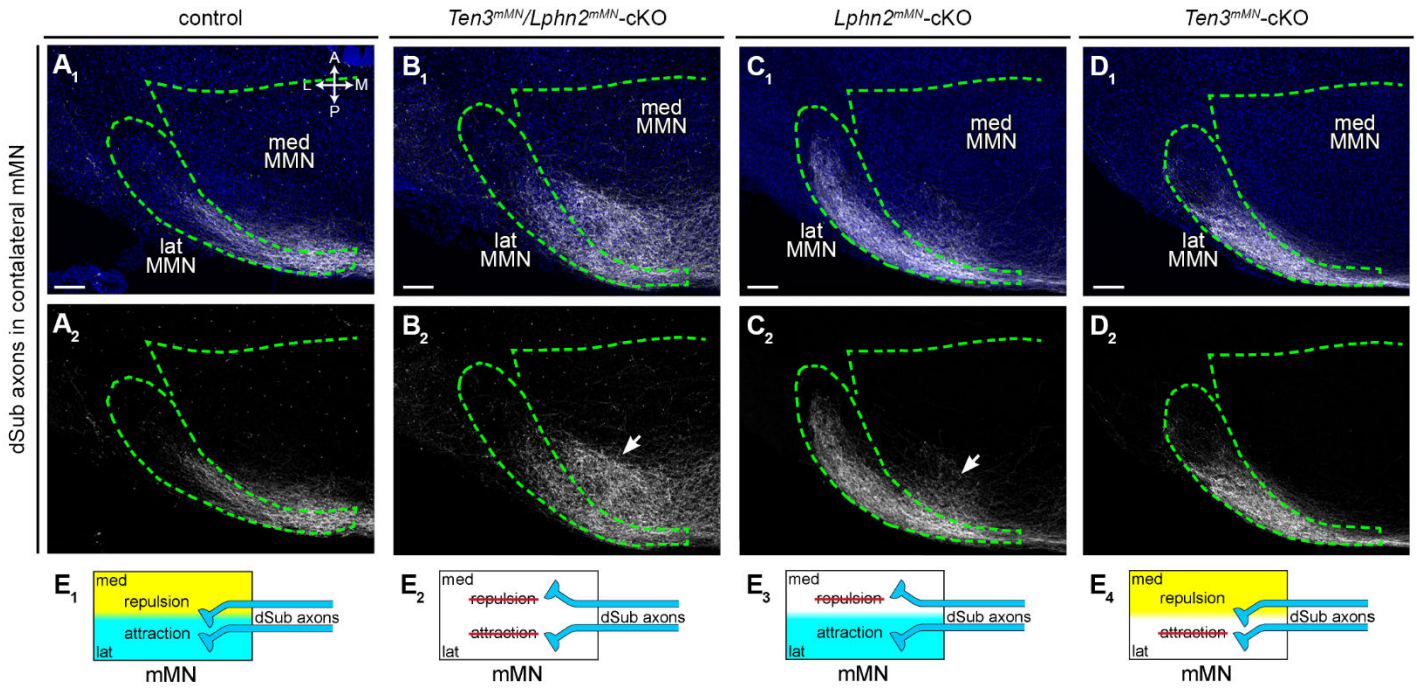

Figure S6. Analysis of contralateral dSub→lat-mMN projections in target deletion conditions, related to Figure 5

(A) Representative images of projection of dSub axons into contralateral medial mammillary nucleus of control mice (A_1). Bottom panel shows axons without DAPI counterstain (A_2). Same animal as Figure 5D, E. Scale bar, 100 µm.

(B–D) Same as A, but for genotypes indicated above. dSub axons in *Ten3*^{mMN}/*Lphn2*^{mMN}-cKO (B) and *Lphn2*^{mMN}-cKO (C) mice spread medially outside of contralateral lat-mMN (arrows in B_2, C_2). Same as animal of corresponding genotype in Figure 5F–K.

(E) Schematic summary of target selection of dSub axons in contralateral mMN when *Ten3* (E_4), *Lphn2* (E_3), or both (E_2) were conditionally knocked out in mMN.

				P0		Adult	
Figure	**Panel**	**Genotype**	**Designation**	**Region**	**Virus**	**Region**	**Virus/Tracer**
Figure 1	**B**	*Ten3$^{HA/HA}$;Lphn2$^{mVenus/mVenuss}$*	—	—	—	—	—
	C	wildtype	—	—	—	dSub pSub	*AAV8-ChR2-mCherry* *AAV8-ChR2-GFP*
Figure 2	**C–D**	CD1 wildtype	control (*Ten3$^{+/+}$*)	MEC	*LV-CAG-Cre-GFP*	MEC	*AAV8-CreON-GFP* *AAV8-CreOFF-mCherry*
	E–F, K–L	*Ten3$^{fl/fl}$*	*Ten3^{MEC}-cKO*	MEC	*LV-CAG-Cre-GFP*	MEC	*AAV8-CreON-GFP* *AAV8-CreOFF-mCherry*
Figure 3	**A**	*Nts-Cre;Ai75D/+*	*Nts-Cre;LSL-ntdT* [1]	—	—	—	—
	D–E	*Ten3$^{fl/fl}$;Lphn2$^{fl/fl}$*	control	—	—	MEC	*AAV8-CreOFF-mCherry*
	F–G	*Nts-Cre;Ten3$^{fl/fl}$;Lphn2$^{fl/fl}$*	*Ten3^{Sub}/Lphn2^{Sub}*-cKO	—	—	MEC	*AAV8-CreOFF-mCherry*
	H–I	*Nts-Cre;Ten3$^{+/+}$;Lphn2$^{fl/fl}$*	*Lphn2^{Sub}*-cKO	—	—	MEC	*AAV8-CreOFF-mCherry*
	J–K	*Nts-Cre;Ten3$^{fl/fl}$;Lphn2$^{+/+}$*	*Ten3^{Sub}*-cKO	—	—	MEC	*AAV8-CreOFF-mCherry*
Figure 4	**C–D**	*Nts-Cre;Ten3$^{+/+}$*	control	—	—	dSub	*AAV8-CreON-mCherry*
	E–F, I	*Nts-Cre;Ten3$^{fl/fl}$*	*Ten3^{Sub}*-cKO	—	—	dSub	*AAV8-CreON-mCherry*
Figure 5	**A**	*Sim1-Cre;Ai75D/+*	*Sim1-Cre;LSL-ntdT* [1]	—	—	—	—
	D–E	*Ten3$^{fl/fl}$;Lphn2$^{fl/fl}$*	control	—	—	dSub	*AAV8-ChR2-mCherry*
	F–G	*Sim1-Cre;Ten3$^{fl/fl}$;Lphn2$^{fl/fl}$*	*Ten3^{mMN}/Lphn2^{mMN}*-cKO	—	—	dSub	*AAV8-ChR2-mCherry*
	H–I	*Sim1-Cre;Ten3$^{+/+}$;Lphn2$^{fl/fl}$*	*Lphn2^{mMN}*-cKO	—	—	dSub	*AAV8-ChR2-mCherry*
	J–K	*Sim1-Cre;Ten3$^{fl/fl}$;Lphn2$^{+/+}$*	*Ten3^{mMN}*-cKO	—	—	dSub	*AAV8-ChR2-mCherry*
Figure 6	**C–D**	*Nts-Cre;Lphn2$^{+/+}$*	control	—	—	pSub	*AAV8-CreON-GFP*
	E–F, I	*Nts-Cre;Lphn2$^{fl/fl}$*	*Lphn2^{Sub}*-cKO	—	—	pSub	*AAV8-CreON-GFP*
Figure 7	**C–D**	*Ten3$^{fl/fl}$;Lphn2$^{fl/fl}$*	control	—	—	pSub	*AAV8-ChR2-GFP*
	E–F, I	*Sim1-Cre;Ten3$^{fl/fl}$;Lphn2$^{fl/fl}$*	*Ten3^{mMN}/Lphn2^{mMN}*-cKO	—	—	pSub	*AAV8-ChR2-GFP*
Sup. Figure 1	**C**	CD1 wildtype	—	MEC	Biocytin TMR[2]	—	—
	D	*Ten3$^{HA/HA}$;Lphn2$^{mVenus/mVenuss}$*	—	MEC	Biocytin TMR[2]	—	—
	E–F	*Ten3$^{HA/HA}$;Lphn2$^{mVenus/mVenuss}$*	—	—	—	—	—
Sup. Figure 2	**C–D**	CD1 wildtype	control (*Ten3$^{+/+}$*)	MEC	*LV-CAG-Cre-GFP*	MEC	*AAV8-CreON-GFP* *AAV8-CreOFF-mCherry*
	E–F, K–L	*Ten3$^{fl/fl}$*	*Ten3^{MEC}-cKO*	MEC	*LV-CAG-Cre-GFP*	MEC	*AAV8-CreON-GFP* *AAV8-CreOFF-mCherry*
Sup. Figure 3	**A–C**	*Nts-Cre;Ai75D/+*	*Nts-Cre;LSL-ntdT*	—	—	—	—
	D–E	*Sim1-Cre;Ai75D/+*	*Sim1-Cre;LSLn-ntdT*	—	—	—	—
Sup. Figure 4	**A**	*Ten3$^{fl/fl}$;Lphn2$^{fl/fl}$*	control	—	—	MEC	*AAV8-CreOFF-mCherry*
	B	*Nts-Cre;Ten3$^{fl/fl}$;Lphn2$^{fl/fl}$*	*Ten3^{Sub}/Lphn2^{Sub}*-cKO	—	—	MEC	*AAV8-CreOFF-mCherry*
Sup Figure 5	**A–B**	*Nts-Cre;Ten3$^{+/+}$*	control	—	—	dSub	*AAV8-CreON-mCherry*
	C–D	*Nts-Cre;Ten3$^{fl/fl}$*	*Ten3^{Sub}*-cKO	—	—	dSub	*AAV8-CreON-mCherry*
Sup. Figure 6	**A**	*Ten3$^{fl/fl}$;Lphn2$^{fl/fl}$*	control	—	—	dSub	*AAV8-ChR2-mCherry*
	B	*Sim1-Cre;Ten3$^{fl/fl}$;Lphn2$^{fl/fl}$*	*Ten3^{mMN}/Lphn2^{mMN}*-cKO	—	—	dSub	*AAV8-ChR2-mCherry*
	C	*Sim1-Cre;Ten3$^{+/+}$;Lphn2$^{fl/fl}$*	*Lphn2^{mMN}*-cKO	—	—	dSub	*AAV8-ChR2-mCherry*
	D	*Sim1-Cre;Ten3$^{fl/fl}$;Lphn2$^{+/+}$*	*Ten3^{mMN}*-cKO	—	—	dSub	*AAV8-ChR2-mCherry*

[1] ***LSL-****ntdT = CAG promoter-loxP-stop-loxP-nucleus-targeted tdTomato* in the *Rosa26* locus (a nuclear Cre reporter designated as *Ai75D*)

[2] Biocytin TMR [5-(and-6)-tetramethylrhodamine biocytin] was injected in several time points around birth, rather than exclusively P0

Table S1. Summary of genotypes and viruses in each experiment, arranged according to figure panel.